Supplementary Information (SI) for Journal of Materials Chemistry A.

Morphology Tuned Viologen Based Covalent Organic Frameworks: A Fast and Targeted Approach to Eliminate Toxic Organic Pollutants from Water

Pampa Jhariat,[b] *Arjun Warrier,*[b] *Mebin Varghese*[b] *and Tamas Panda* * [a]

[a] Centre for Clean Environment, Vellore Institute of Technology, Vellore, Tamil Nadu-632014, India

[b] Department of Chemistry, School of Advanced Sciences, Vellore Institute of Technology, Vellore, Tamil Nadu-632014, India.

Table of Contents

Section SI. General information

SI: General Information

Instruments:

- **Fourier transform infrared (FT-IR) spectra:** Fourier transform infrared (FT-IR) spectra were recorded on IRAffinity-1 (Shimadzu, Japan) spectrometer at Zn-Se ATR (attenuated total reflection) mode in the 4000-400 cm $^{-1}$ (mid-IR range) region.

- **Powder X-ray diffraction (PXRD):** Bruker D8 Advanced XRD (excitation source: 2.2KW Cu-anode ceramic tube) was used for analyzing the PXRD pattern of all the vCOFs. We have further processed the PXRD data by using the X'pert High Score Plus software for background correction.

- **Thermogravimetric analyses (TGA):** Thermo-gravimetric analysis (TGA) was conducted using an SDT Q600 TG-DTA analyzer under a nitrogen atmosphere, with measurements recorded from 25 to 800 °C. The heating rate employed was 20 °C min^{-1}

- **Gas adsorption (BET Surface area):** Adsorption isotherms were obtained using a Quantachrome USA device at 77 K, which was maintained by liquid nitrogen. Before the analysis, the vCOFs samples were degassed for 12 hours at 100 °C in the presence of liquid nitrogen

- **Field Emission - Scanning Electron Microscopy (FE-SEM):** The Thermo Fisher FEI QUANTA 250 FEG was used for the FE-SEM analysis the morphological diversity of the four vCONs. The Instrument is equipped with the Schottky Field Emission Electron Gun as source of Electrons with an operating voltage range of 5kV-30kV offering high resolution of 1.2 nm at 30 kV at high vacuum conditions.

- **High-Resolution Transmission Electron Microscope (HR-TEM**): FEI-TECNAI-G2 20 TWIN was used for the HR-TEM analysis of vCOFs.

- **Nuclear Magnetic Resonance Spectroscopy:** Magic Angle Spinning (MAS) solid-state NMR experiments for vCOFs were carried out on a 500 MHz BRUKER AVANCE NEONMR spectrometer. NMR data were processed using Top-Spin software.

- **Atomic Force Microscopy (AFM):** Atomic Force Microscopy images were recorded on the NaioAFM instrument in noncontact mode. The samples were evenly coated on glass slides using a Spin coater (Soin Coating Unit Holmarc, India) with 3000rpm rotation speed for 2 min.

- **Gonimeter:** Water contact angle measurements of vCOFs were conducted using the Phoenix 300 instrument from SEO, Korea.

- **UV-Vis Spectrophotometer:** JASCO V-750 SPECTROPHOTOMETER was used to record the UV graphs for the capture study of organic pollutants.

- **Confocal Microscopy:** Confocal Laser Scanning Microscope- Fluoview Fv3000 (Olympus, Japan) was used to capture dye-captured vCOFs images.

SII: Methodology and Material Characterization:

1. Synthesis of vCOFs (vBPDP and vMEL):

Viologen-based vBPDP and vMEL were synthesized using a template-free solvothermal-assisted Zincke reaction. Initially, the Zincke salt L1 [1,1′-bis(2,4-dinitrophenyl)-[4,4′-bipyridine]-1,1-diium dichloride, 0.5 mmol] was mixed separately with the respective triamine, either N,N'-bis(4-aminophenyl)benzene-1,4-diamine (BPDP, 0.5 mmol) or melamine (MEL, 0.5 mmol), in a solution mixture within a sealed Pyrex glass tube under a nitrogen atmosphere. The mixtures underwent three freeze-pump-thaw cycles before being heated at 120 °C for 72 hours. Various solvent mixtures were tested during the solvothermal reaction (Table S1, Section: VII) to achieve a pure phase of vMEL and vBPDP (Table S1). Pure products were successfully synthesized using two solvent systems: dioxane and water (2:1) and mesitylene and water (4:1). Products synthesized in dioxane: water were designated as vMEL-7 and vBPDP-7, while those synthesized in mesitylene: water was denoted as vMEL-8 and vBPDP-8. After completing the reaction, the precipitates were collected via centrifugation and vacuum filtration. The samples were thoroughly washed with polar solvents such as dimethylformamide (DMF), dimethylacetamide (DMAc), ethanol (EtOH), boiling water, methanol (MeOH), dichloromethane (DCM), and acetone to remove small polymers, oligomers, and impurities. Following the washing process, the products were immersed in a chloroform and tetrahydrofuran (1:1) solution for three days to exchange high-boiling solvents for low-boiling ones. Finally, the purified products were recovered through vacuum filtration and dried overnight at 100 °C.

Abirritations: *MEL- Melamine, L1- 1,1'-bis(2,4-dinitrophenyl)-[4,4'-bipyridine]-1,1-diium dichloride, BPDP- N,N'-bis(4-aminophenyl)benzene-1,4-diamine*

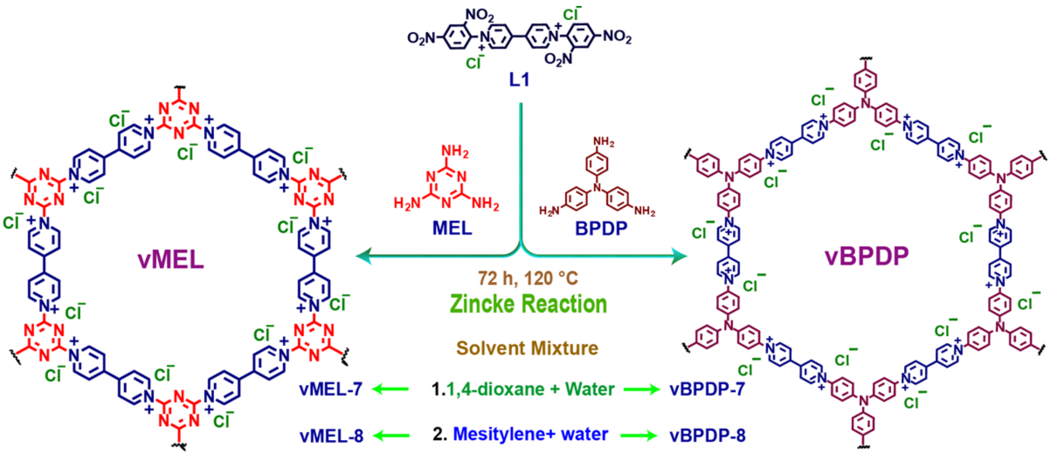

Figure S1: Synthesis scheme of vMEL and vBPDP COF by the solvothermal assisted Zincke reaction. Two combinations of the solvent mixture were used in reaction, i.e. first, 1,4-dioxane+ water (products denoted as vMEL-7 and vBPDP-7) and second, Mesitylene+ water (products denoted as vMEL-8 and vBPDP-8)

2. Material Characterization:

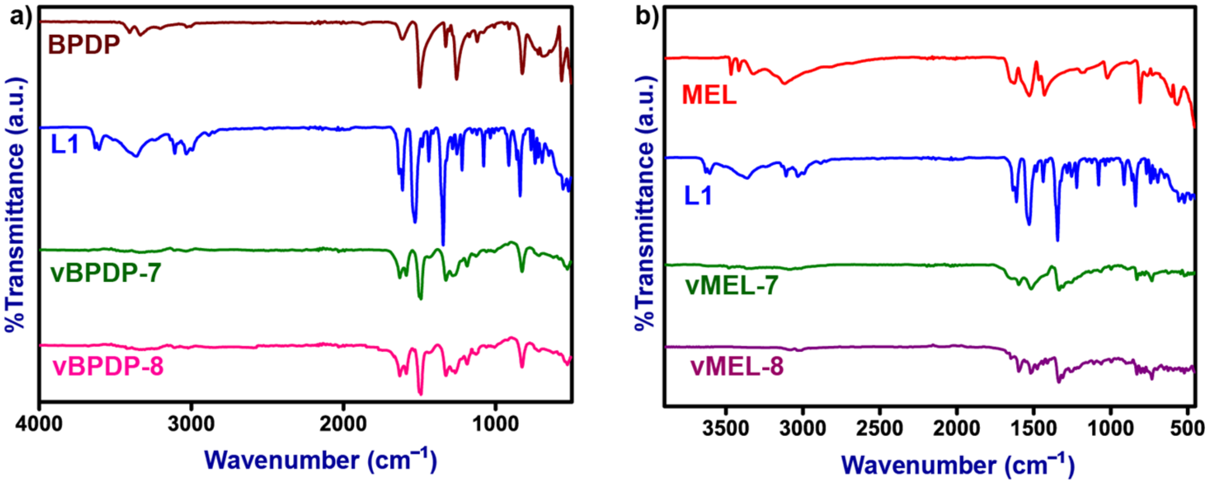

Figure S2: FT-IR spectra of a) vBPDP and b) vMEL, compared with their respective starting organic linker (L1), and respective triamine (BPDP and MEL). The disappearance of symmetric and asymmetric stretching peaks of NO_2 groups at 1550 cm^{-1} and 1365 cm^{-1} respectively, confirms the reduction of 2,4-dinitroaniline and assures the formation of the desired product.

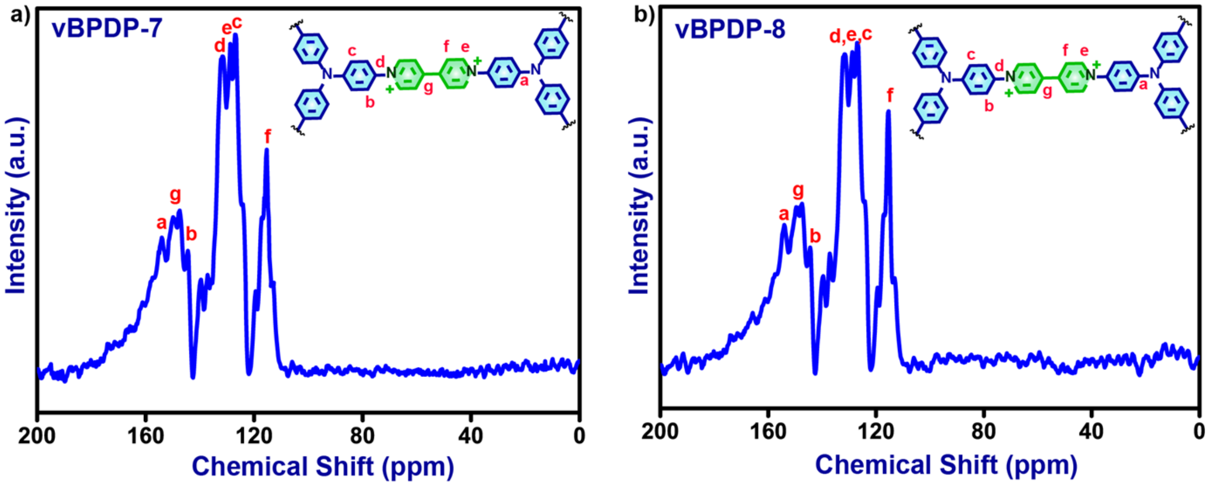

Figure S3: Solid state ^{13}C-NMR spectra of a) vBPDP-7 and b) vBPDP-8.

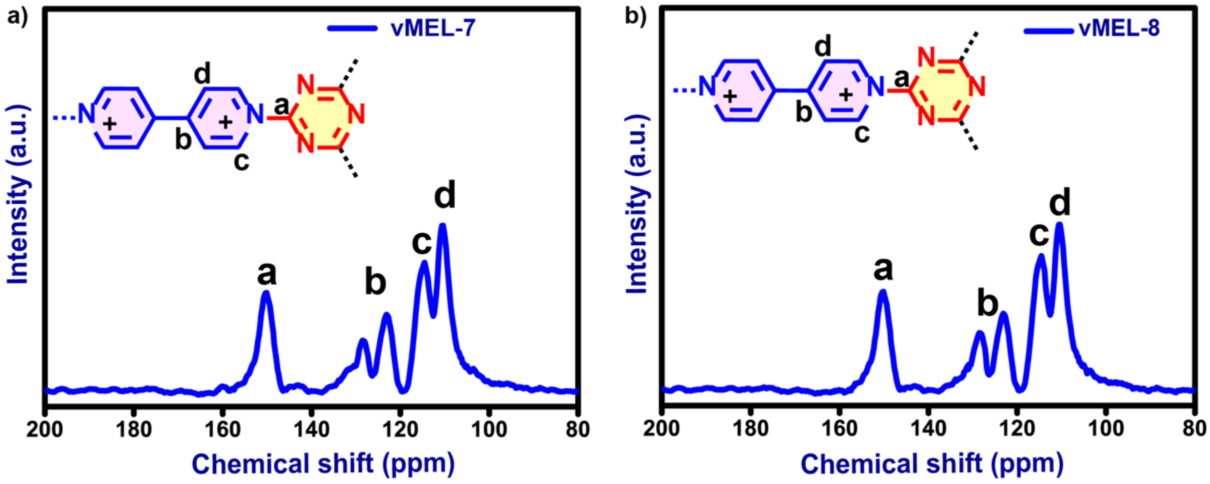

Figure S4: Solid state ^{13}C-NMR spectra of a) vMEL-7 and b) vMEL-8.

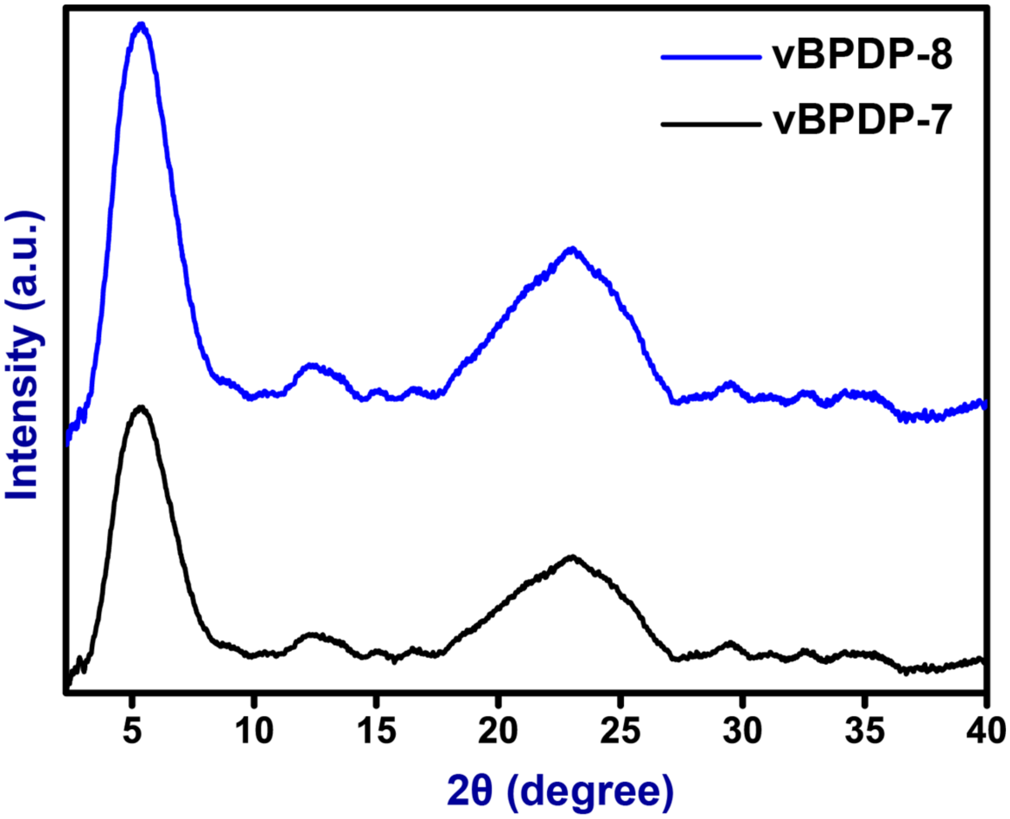

Figure S5: Experimental Powder Xray diffraction pattern of as synthesized vBPDP COF.

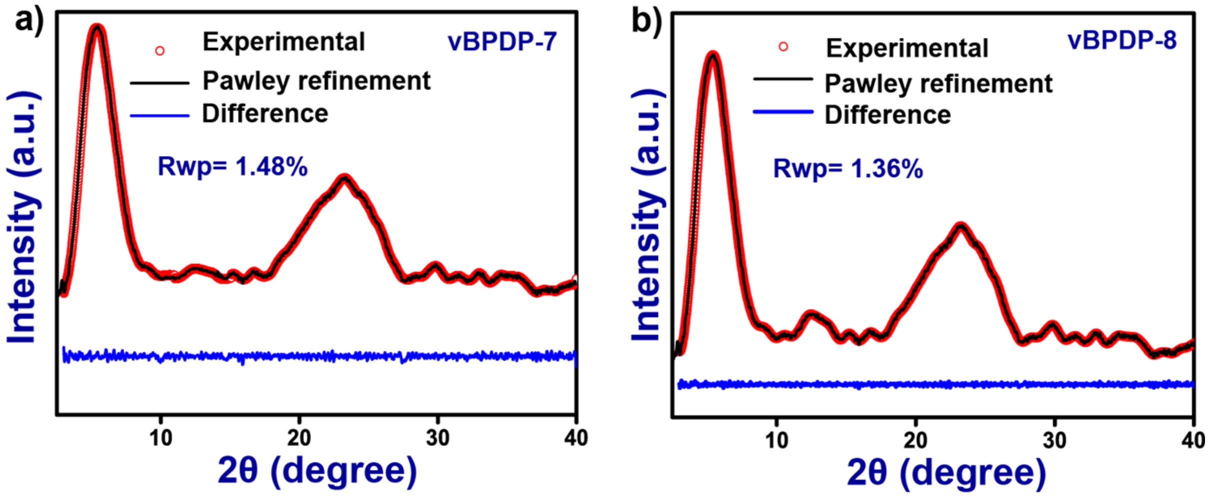

Figure S6: Powley refinement of simulated vBPDP structure with the experimental powder pattern of a) vBPDP-7 (R_{wp} is 1.48%) and b) vBPDP-8 (R_{wp} is 1.36%).

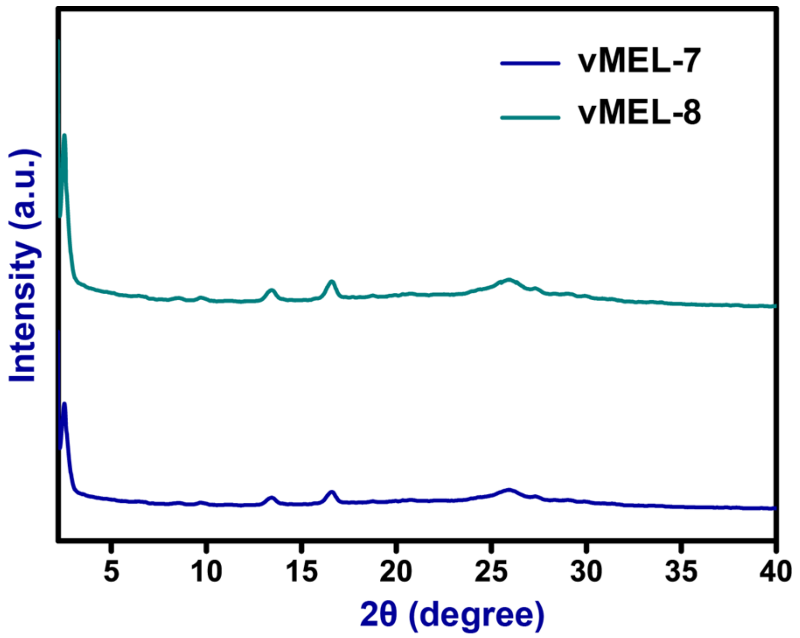

Figure S7: Experimental Powder Xray diffraction pattern of as synthesized vMEL COF.

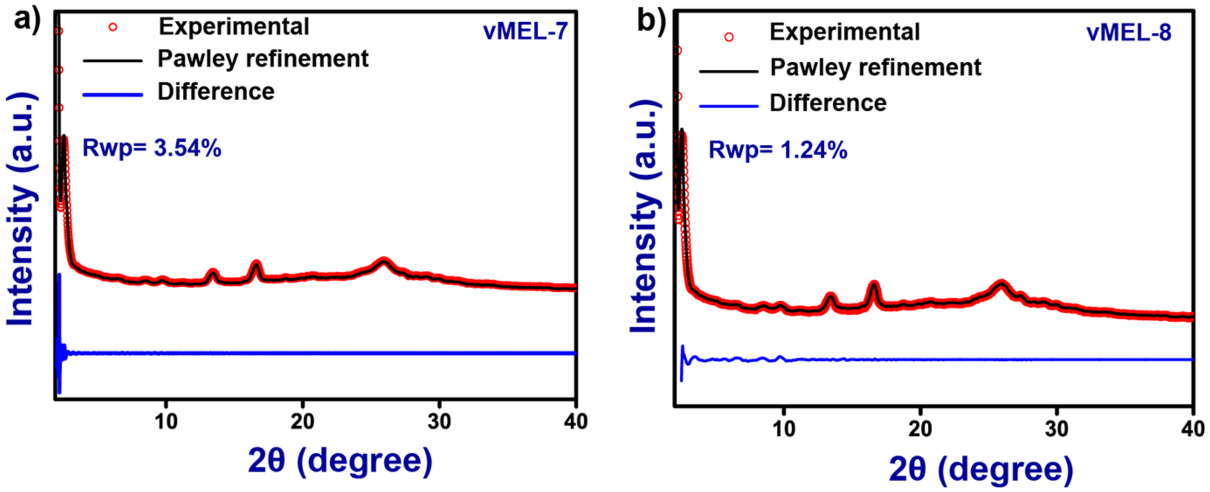

Figure S8: Powley refinement of simulated vMEL structure with the experimental powder pattern of a) vMEL-7 (R_{wp} is 3.54%) and b) vMEL-8 (R_{wp} is 1.24%).

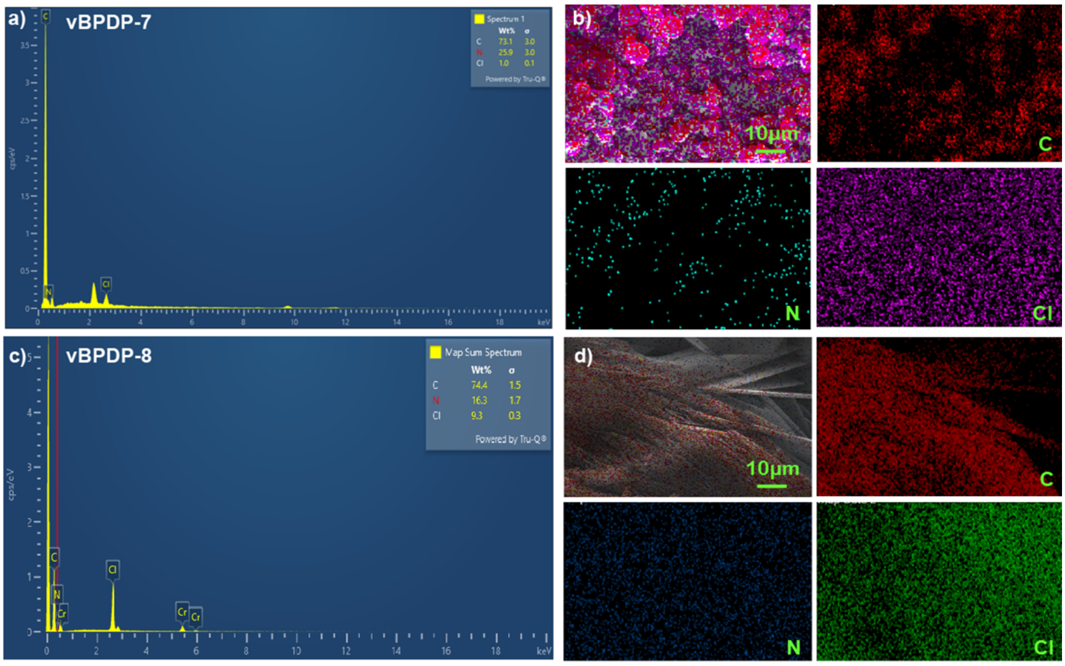

Figure S9: FESEM-EDAX and FESEM EDX elemental mapping of a) vBPDP-7 and b) vBPDP-8. Inset of each figure showed the percentage of C, N, O and Cl content

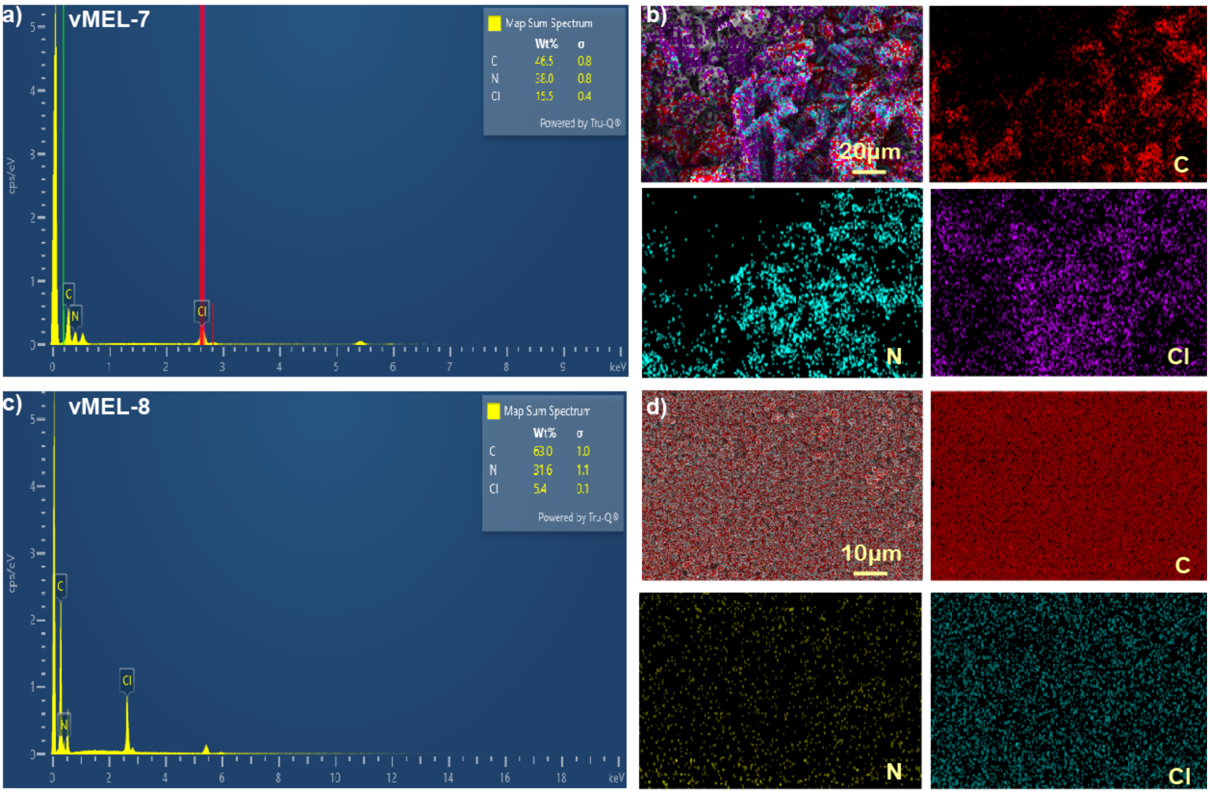

Figure S10: FESEM-EDAX and FESEM EDX elemental mapping of a) vMEL-7 and b) vMEL-8. Inset of each figure showed the percentage of C, N, O and Cl content

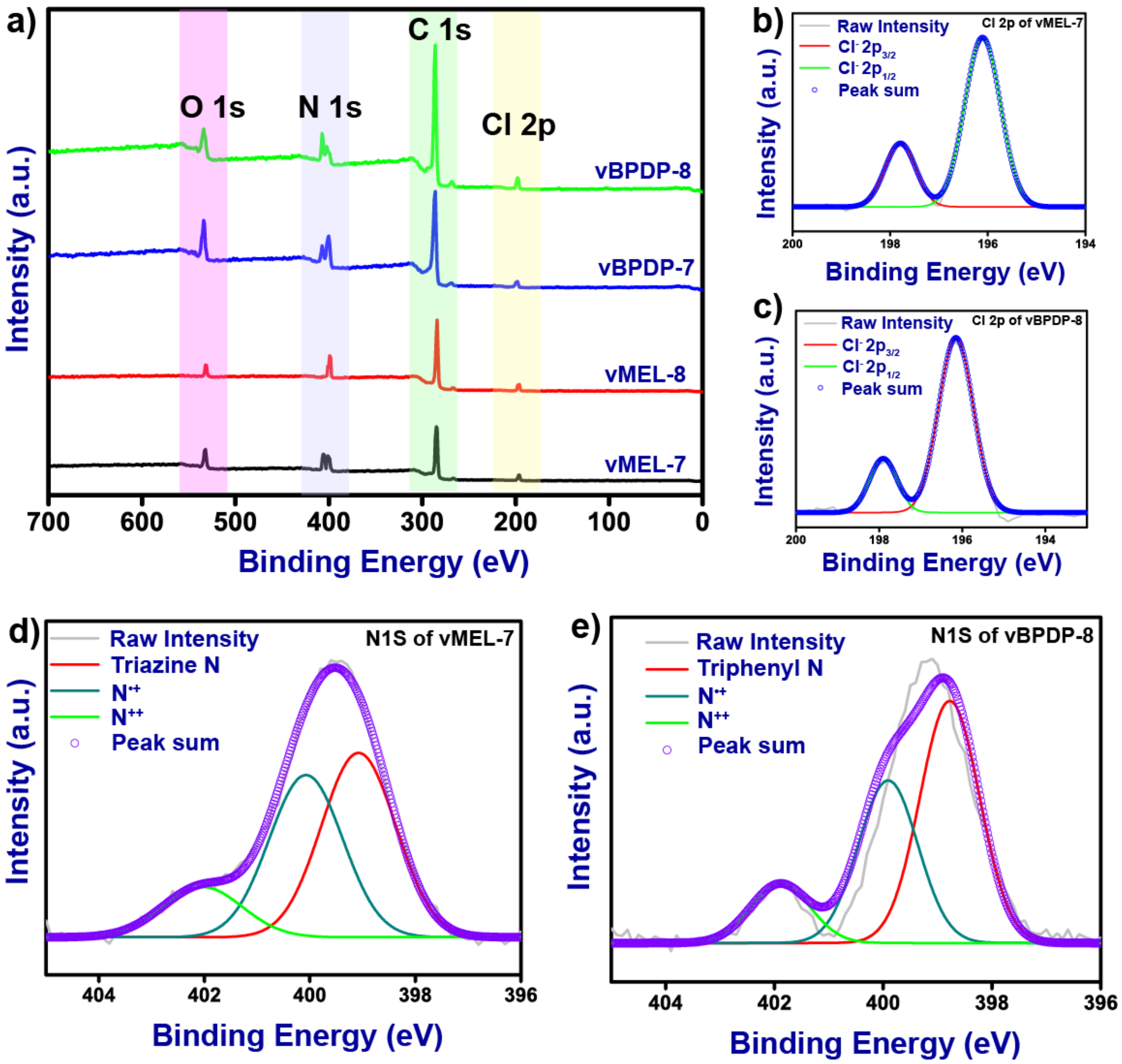

Figure S11: XPS spectra of all vCOFs. a) Combined survey scan of all vCOFs. Represented the Cl 2p XPS spectra of b) vMEL-7 and c) vBPDP-8. Represented the N1s XPS spectra of d) vMEL-7 and e) vBPDP-8.

SIII: Morphological Diversity in vCOFs:

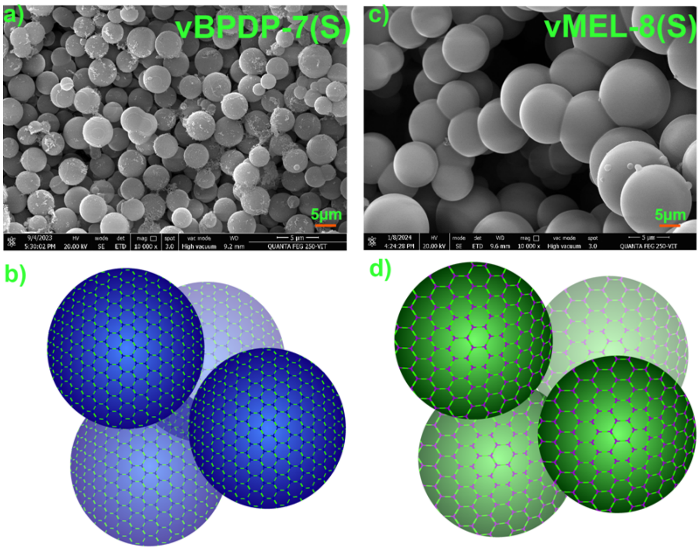

Figure S12: FESEM-micrographs of a) vBPDP-7(S) and c) vMEL-8(S). Schematic representation of spherical morphology b) vBPDP-7(S) and d) vMEL-8(S). For BPDP, the solvent mixture of 1,4-dioxane and water resulted in a spherical morphology [vBPDP-7(S)], while for MEL, the solvent mixture of mesitylene and water produced a spherical morphology [vMEL-8(S)].

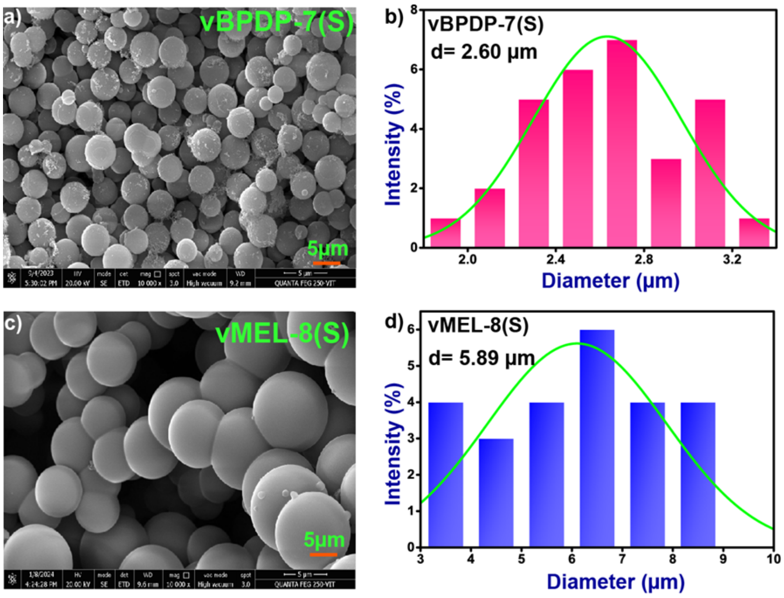

Figure S13: FESEM-micrographs of a) vBPDP-7(S) and c) vMEL-8(S). Particle size distribution of b) vBDPP-7(S) and d) vMEL-8(S) from FESEM images

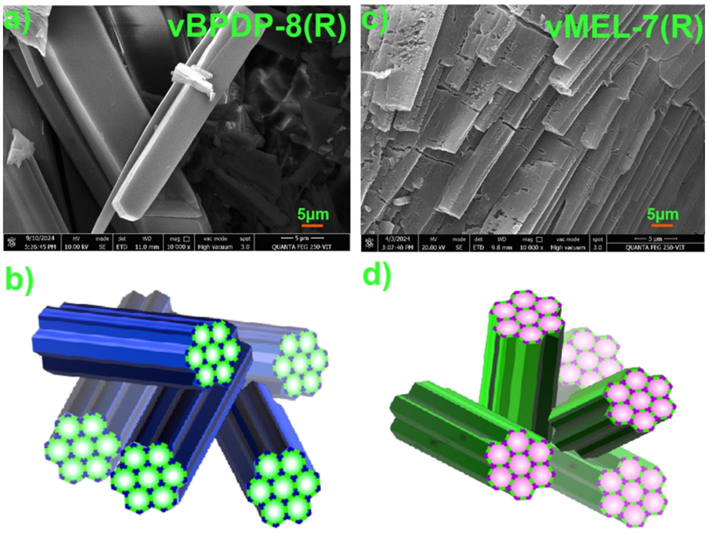

Figure S14: FESEM-micrographs of a) vBPDP-8(R) and c) vMEL-7(R). Schematic representation of rod morphology b) vBPDP-8(R) and d) vMEL-7(R). For BPDP, the solvent mixture of mesitylene and water resulted in a spherical morphology [vBPDP-8(R)], while for MEL, the solvent mixture of 1,4-dioxane and water produced a spherical morphology [vMEL-7(R)].

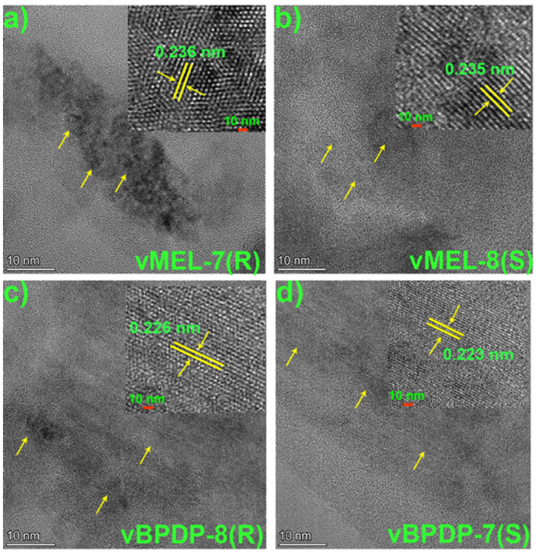

Figure S15: HRTEM Images of vCOFs. Lattice fringes with interplanar distances of a) vMEL-7(R)~ 0.236nm, b) vMEL-8(S)~ 0.235 nm, c) vBPDP-8(R) ~ 0.226 nm and d) vBPDP-7(S)~ 0.223 nm were observed

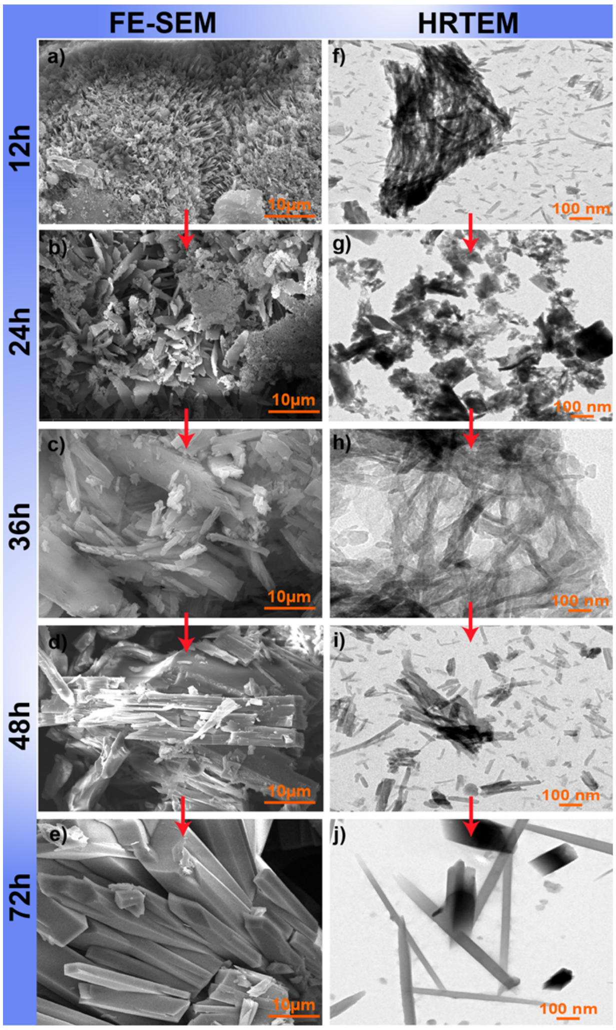

Figure S16: Mechanistic Insite in the formation of rod-shaped morphology in vBPDP-8(R). At different intervals of time (12h, 24h, 36h, 48h and 72h), we recorded the a-e) FE-SEM and f-j) HRTEM micrographs of vBPDP-8(R).

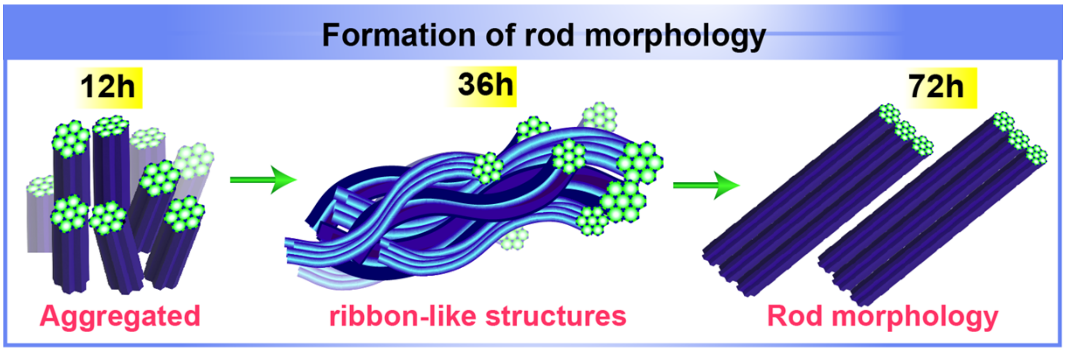

Figure S17: Schematic representation of the formation of rod-shaped morphology in vBPDP-8(R) at different intervals of time (12h, 36h, and 72h).

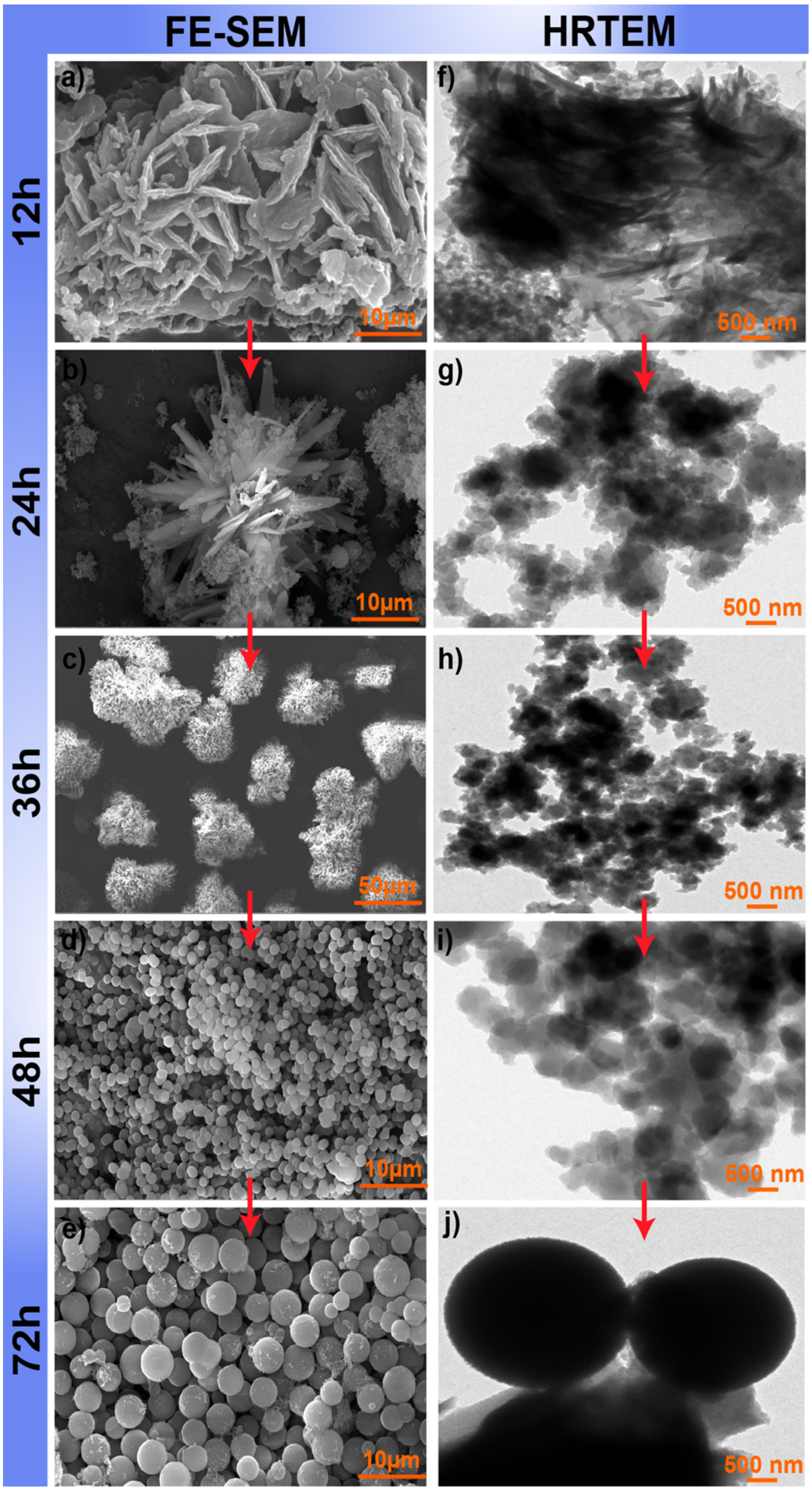

Figure S18a: Mechanistic Insite in the formation of spherical morphology in vBPDP-8(S). At different intervals of time (12h, 24h, 36h, 48h and 72h), we recorded the a-e) FE-SEM and f-j) HRTEM micrographs of vBPDP-8(S).

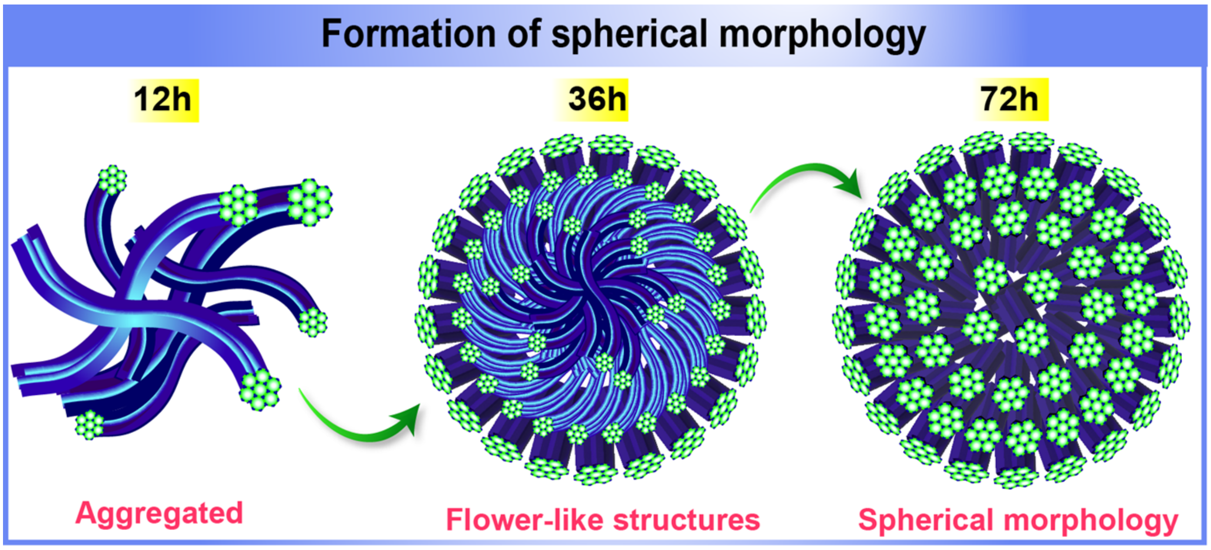

Figure S18b: Schematic representation of the formation of spherical morphology in vBPDP-8(S) at different intervals of time (12h, 36h, and 72h).

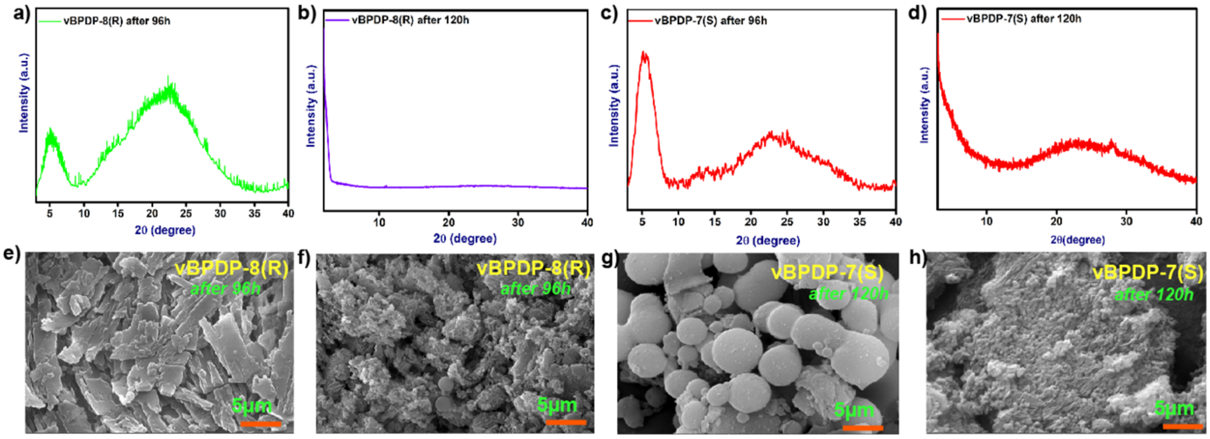

Figure S19: PXRD pattern of vBPDP-8(R) a) after 96h and b) after 120h. PXRD pattern of vBPDP-7(S) c) after 96h and d) after 120h. FESEM micrographs of vBPDP-8(R) e) after 96h and f) after 120h. FESEM micrographs of vBPDP-7(S) g) after 96h and h) after 120h.

SIV: Chemical/Thermal Stability and Surface area measurement:

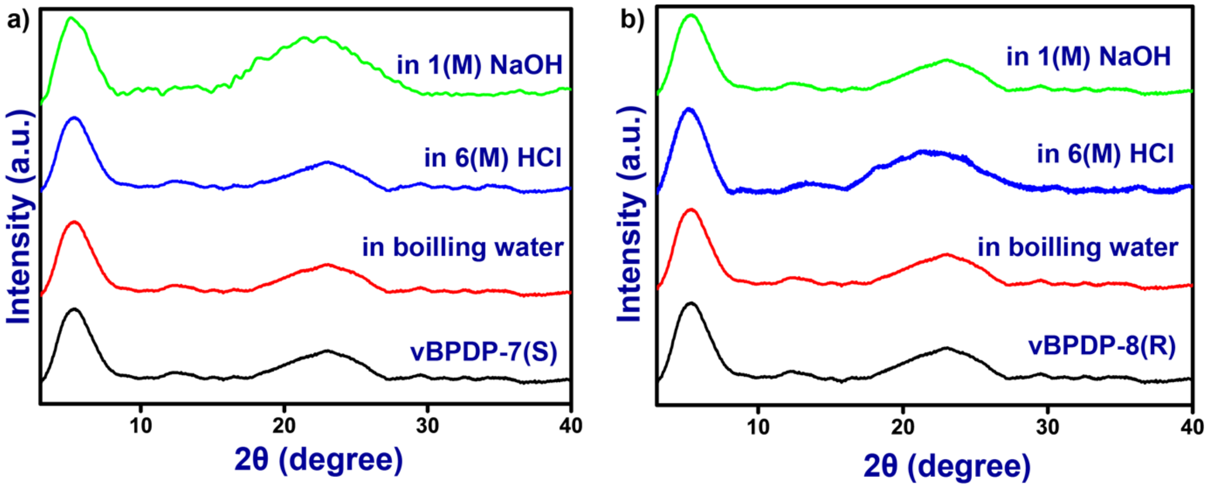

Figure S20: Comparison of the Experimental powder X-ray diffraction patterns of a) vBPDP-7(S) and b) vBPDP-8(R) COF treated with 1 (M) NaOH, 6 (M) HCl and boiling water (100 °C) for 72h.

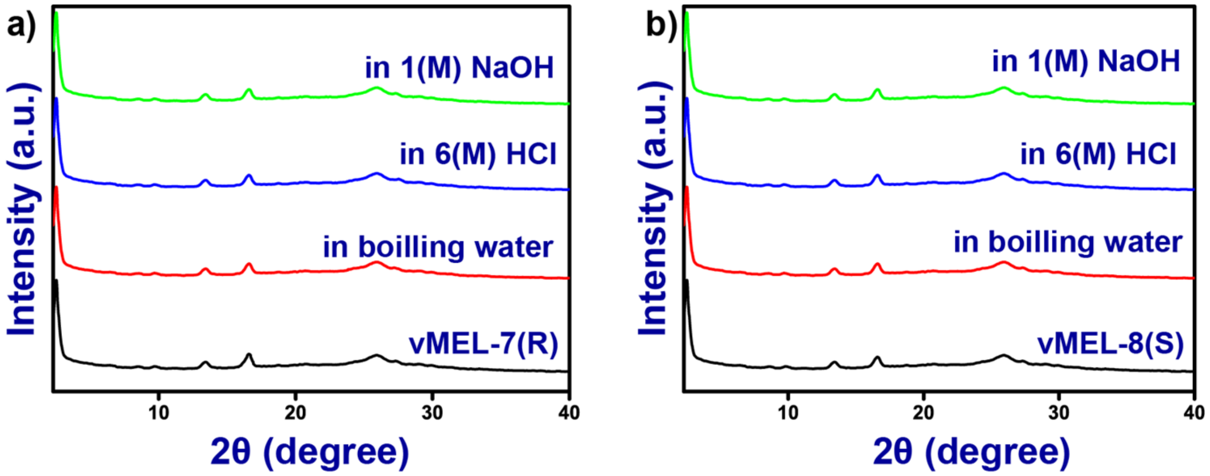

Figure S21: Comparison of the Experimental powder Xray diffraction patterns of a) vMEL-7(R) and b) vMEL-8(S) COF treated with 1 (M) NaOH, 6 (M) HCl and Boling water (100 °C) for 72h.

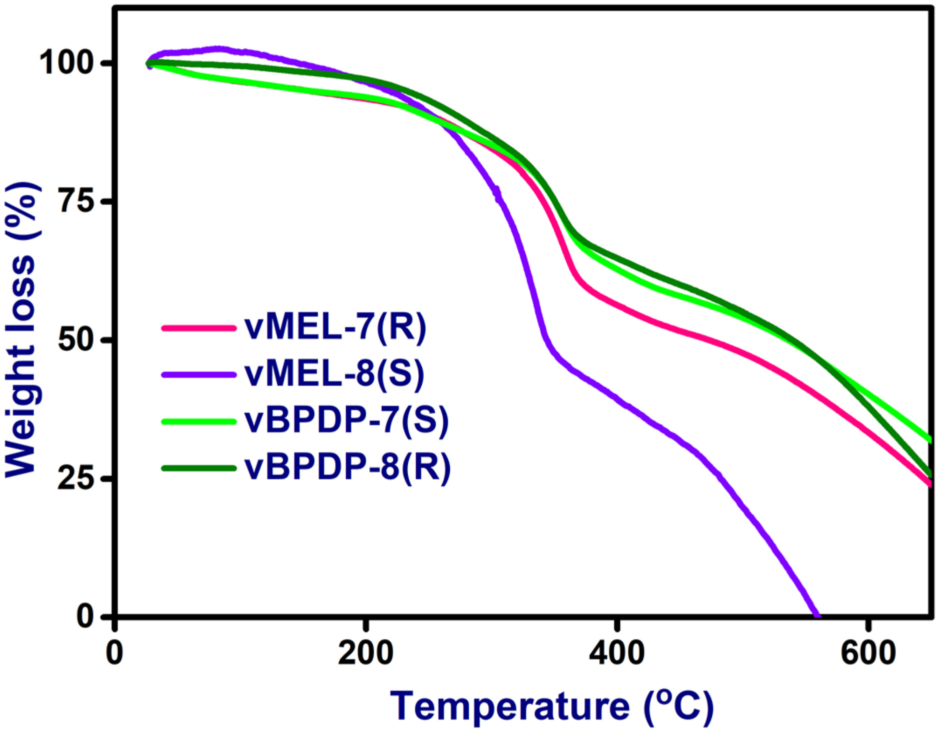

Figure S22: Thermogravimetric analysis of vBPDP-8(R) (olive green line), vBPDP-7(S) (bright green line), vMEL-8(S) (violet line) and vMEL-7(R) (pink line)

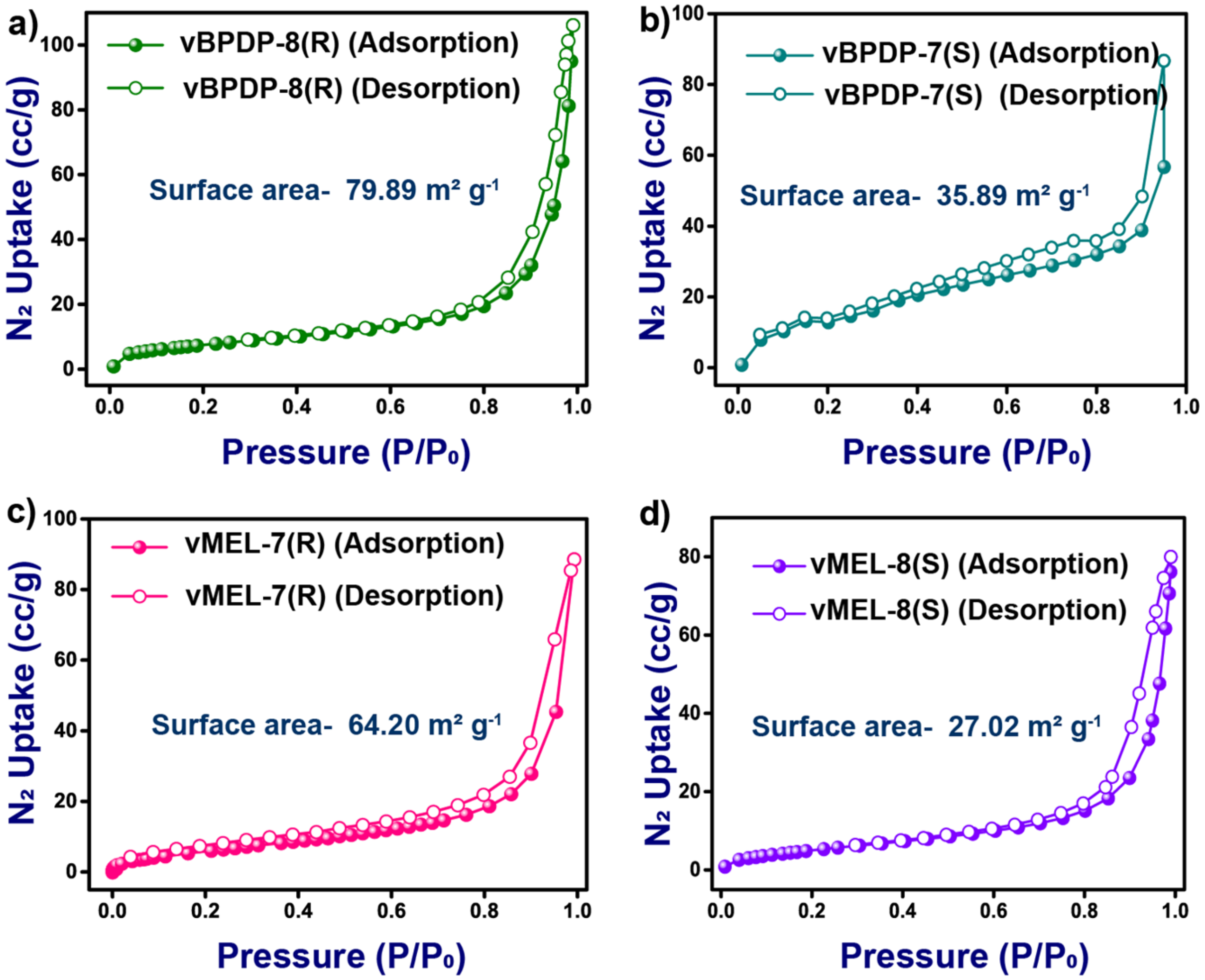

Figure S23: N_2 sorption isotherm curves and BET surface area analysis of a) vBPDP-8(R) (olive green line), b) vBPDP-7(S) (cyan blue line), c) vMEL-7(R) (pink line) and d) vMEL-8(S) (violet line)

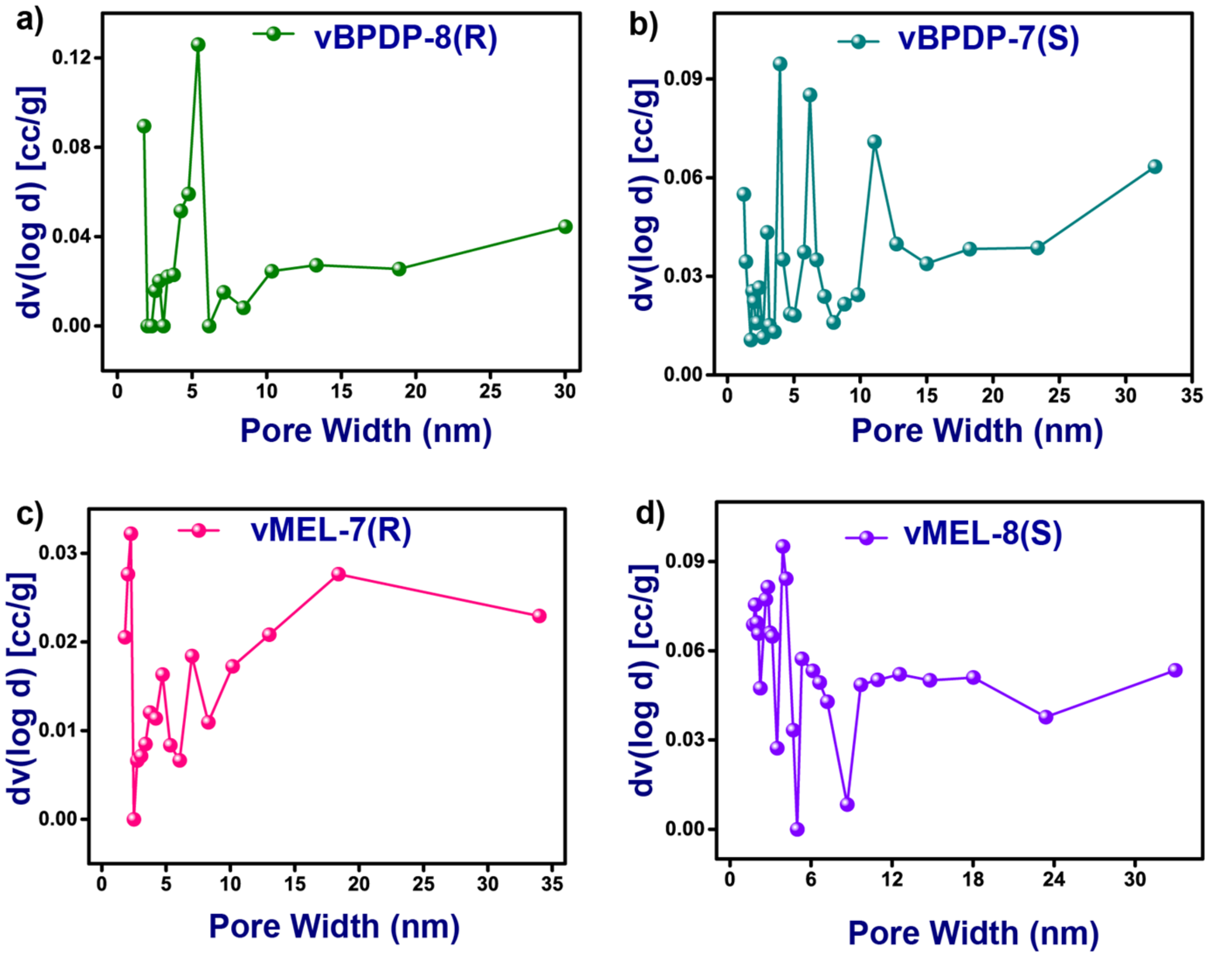

Figure S24: BJH pore size distribution of a) vBPDP-8(R), b) vBPDP-7(S),c) vMEL-7(R) and d) vMEL-8(S).

SV: Capture Study:

Time-Dependent Capture Study/ Kinetics study:

To investigate the uptake kinetics, 2 mg of the samples were dispersed in 5 mL of aqueous dye solutions with an initial concentration of 50 ppm. The solutions were sealed and placed on an orbital shaker at 250 rpm for varying durations (ranging from 10 sec to 10 min). The samples were removed from the solutions and filtered the filter to eliminate suspended particles. The filtered solutions were then analyzed using UV-visible spectroscopy at specific wavelengths (360 nm and 527nm for ARS^-, 498 nm for CR^{2-}, 510 nm for MO^-, 494 nm for FL, 663 nm for MB^+ and 554 nm for RhB^+) to measure the residual dye concentrations at each time point.

$D_t = [\ (C_0\text{-}C_t)/C_0 * 100\ \%] = [\ (A_0\text{-}A_t)/A_0 * 100\ \%]$ …………………(1)

i.e., $C_t = C_0 - (A_0\text{-}A_t)/A_0 * C_0$ ……………………………(2)

Where D_t is the exchange capacity, C_0 and A_0 are the initial concentration and absorbance of the dye solution respectively, and C_t and A_t, are the concentration and absorbance of the dye solution at specific times respectively. Furthermore, kinetics data for all dyes were fitted in a pseudo-second-order model with the help of the following equation,

$Q_t = (k_2 Q_e^2 t) / (1 + k_2 Q_e t)$ ……………..(3)

Where, t is the time in minutes, and Q_t and Q_e are the amounts of adsorbate (mg g^{-1}) on the adsorbent at different time intervals and at equilibrium respectively.

Adsorption Isotherm study:

vBPDP-8(R) (5 mg) was immersed in 5 mL water solution of four dyes having different concentrations (50-1000 ppm). After 24 hours UV-visible spectroscopy was carried out with the supernatant solution and further fitted with the following equation,

Langmuir model, $Q_e = Q_m C_e / Kd + C_e$……………………… (4)

Where Ce (ppm) and Qe (mg gm^{-1}) are the oxo-anion concentration at equilibrium and the amount of dye adsorbed at equilibrium respectively. Qm (mg gm^{-1}) is the maximum amount of dye per unit mass of adsorbent to form a complete monolayer. Kd (mg/L) is a constant related to the affinity of the binding sites.

Adsorption study in different pH:

Other than interfering anions pH range also can be varied in real time applications. The adsorption study at various pH ranging from 1 to 12 were studied and compared with data at pH=7. The pH adjustments were made using 0.1 M HCl and 0.1 M NaOH solutions. 5 mg of vBPDP-8(R) was immersed in 5 mL of dye solution (ARS^- and FL) at different pH were stirred for 60 min at 300 rpm at room temperature. After the completion the solution was filtered. The UV-Visible Spectroscopic studies were carried out to understand the relative removal efficiency of vBPDP-8(R) towards dye removal.

Adsorption Capacity Study:

We calculated the experimental maximum adsorption capacity of the vCOFs towards the dye through the following procedure. The activated 5 mg vCOFs was added to the 10 mL of higher concentration individual dyes and stirred for 12 h in 300 rpm at room temperature. After the completion the filtrate was analyzed using the UV-visible Spectroscopy. in case of UV-vis measurements were carried out the analysis by diluting the solution. Further the maximum adsorption by per gram of vCOFs were analyzed using the following equation.

$Q_m = [(C_0 - C_t) \text{ x } V] / M$……………….(5)

Here Q_m, C_0, C_t, V and M represents the capacity of the adsorbent (mg g^{-1}), the initial concentration of the dye solution (in ppm), the concentration of the dye solution at specific times (in ppm), the volume of the solution (in L) and the mass used for the adsorbent (in g) respectively.

Column Exchange based capture study:

To check the real time applicability of the vBPDP-8(R) a coloumn exchanged adsorption experiment were conducted. The synthesized vBPDP-8(R) was loaded inside the glass coloumn (bed length length ~ 5 cm and diameter ~ 0.75 cm) which act an adsorbent bed for the dye removal. Then both dyes ARS^- (1000 ppm) and FL(1000 ppm) individually passed through the column through the bed. The column eluted solution was collected in different container and the concentration of the respective anions in these solutions were then analyzed using UV-vis spectroscopy.

Regeneration of vBPDP-8(R) and Recyclability Study:

The vBPDP-8(R) packed in the coloumn were regenerated by passing 3M HCl through the column bed followed by acetone. Then the corresponding dye solution was passed through the column to check the performance up to seven cycles**.**

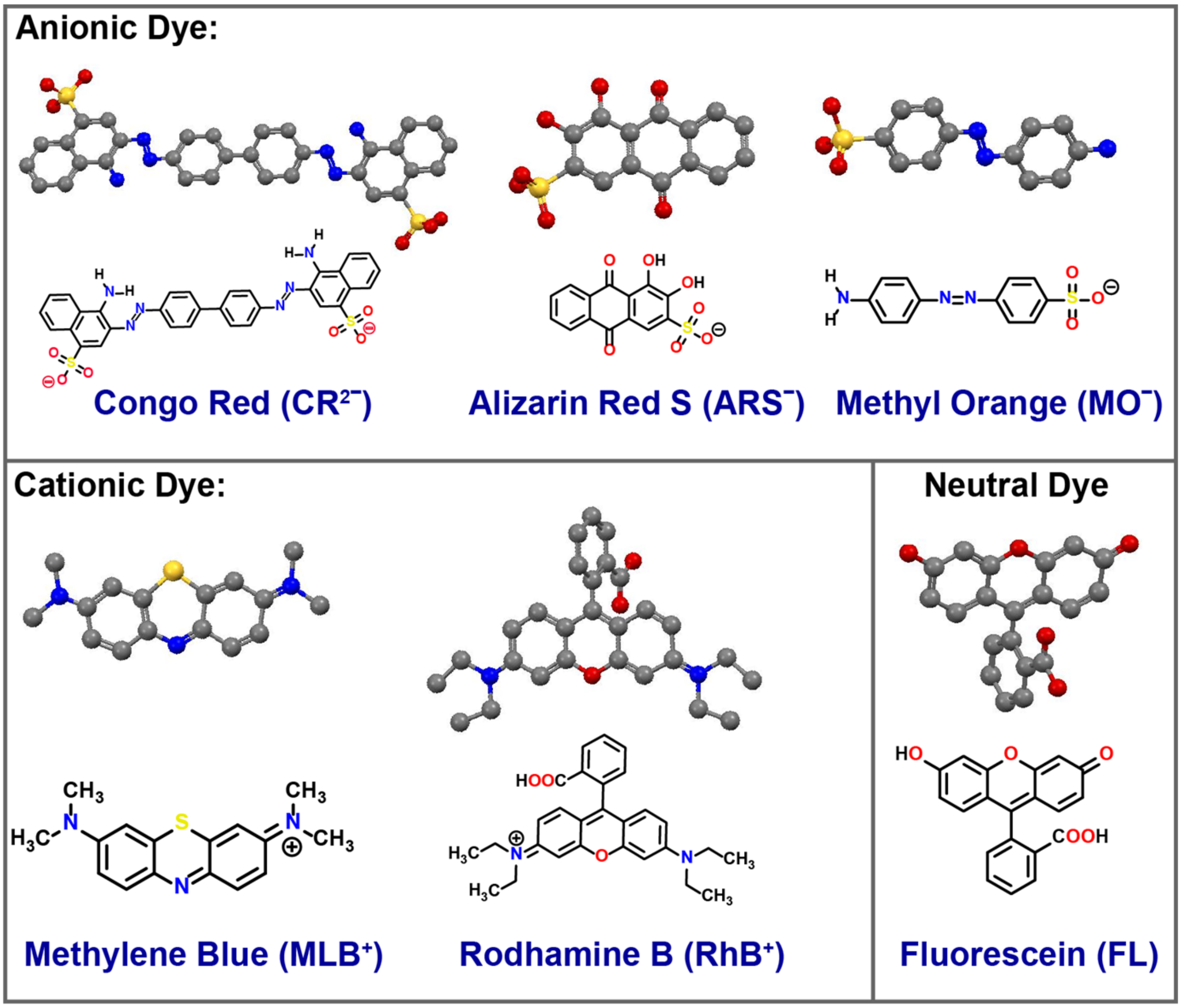

Figure S25: Chemical structures of various organic dye pollutants, used for capture study.

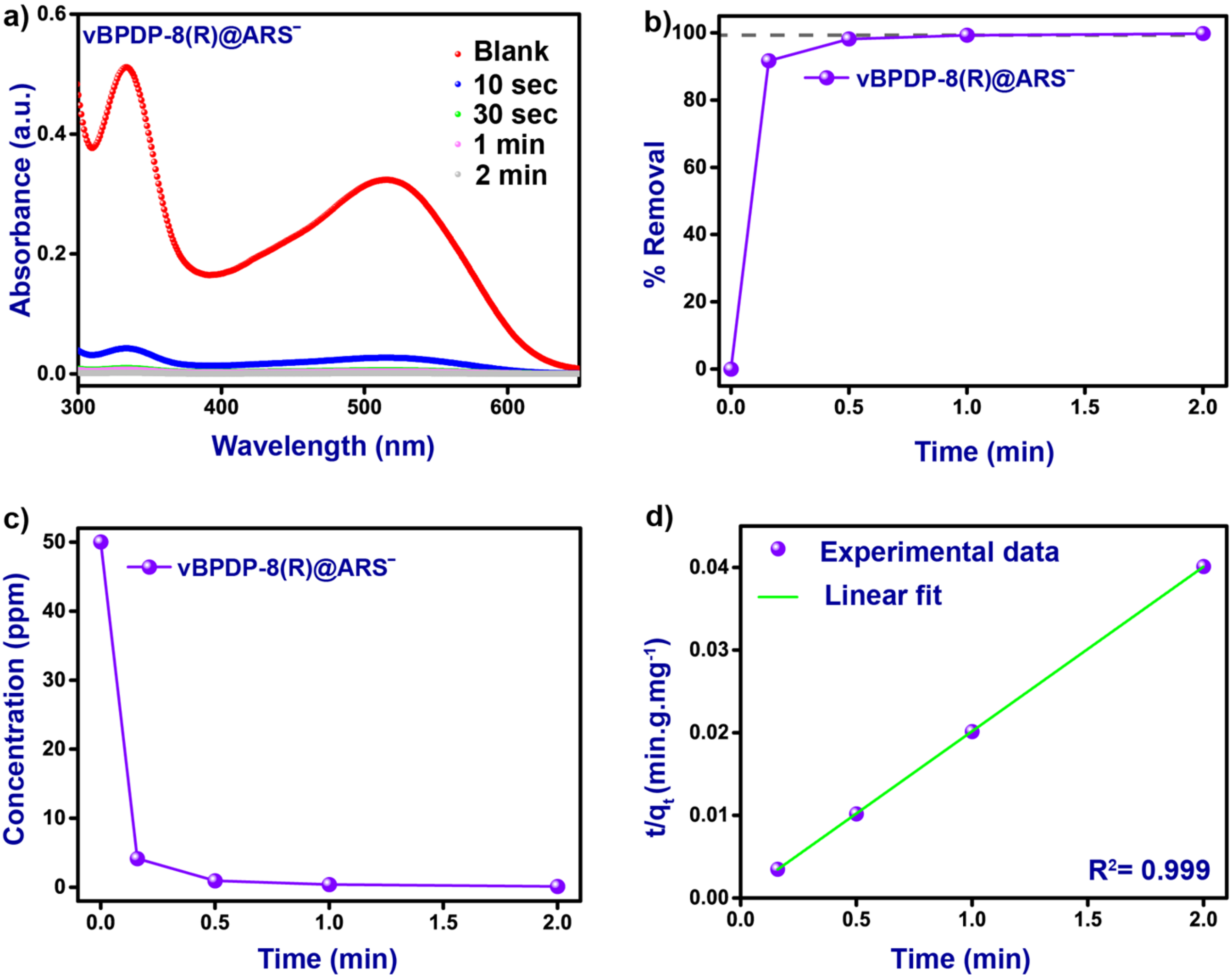

Figure S26: Capture study of Alizarin red S (ARS⁻) via vBPDP-8(R): a) UV-vis spectra of ARS⁻ show diminishing in the absorbance with increasing time, b) % removal vs time, c) Decrease in the concentration with time, d) Pseudo-second-order model fitting for ARS⁻ capture.

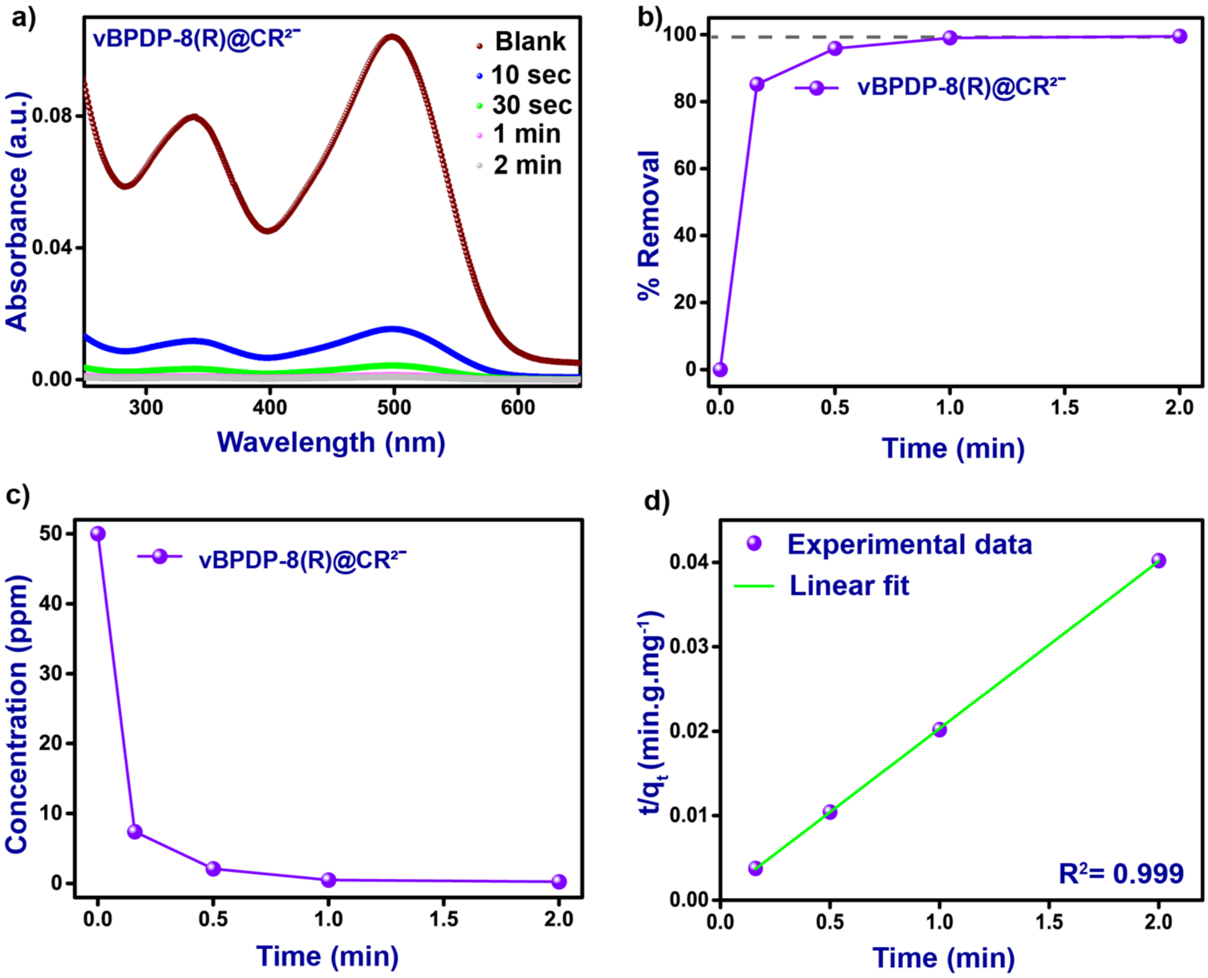

Figure S27: Capture study of Congo red (CR^{2-}) via vBPDP-8(R): a) UV-vis spectra of CR^{2-} show diminishing in the absorbance with increasing time, b) % removal vs time, c) Decrease in the concentration with time, d) Pseudo-second-order model fitting for CR^{2-} capture.

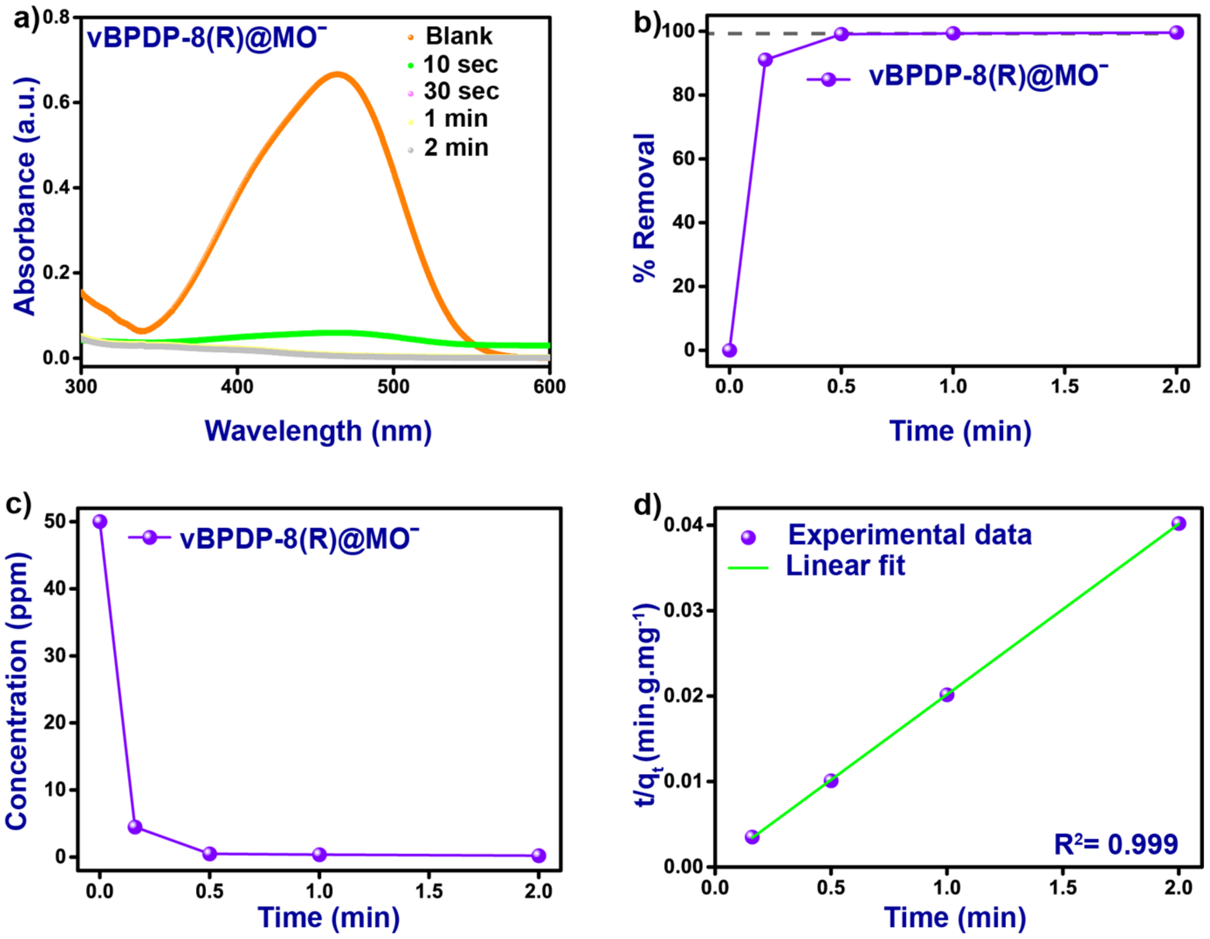

Figure S28: Capture study of Methyl orange (MO^-) via vBPDP-8(R): a) UV-vis spectra of MO^- show diminishing in the absorbance with increasing time, b) % removal vs time, c) Decrease in the concentration with time, d) Pseudo-second-order model fitting for MO^- capture.

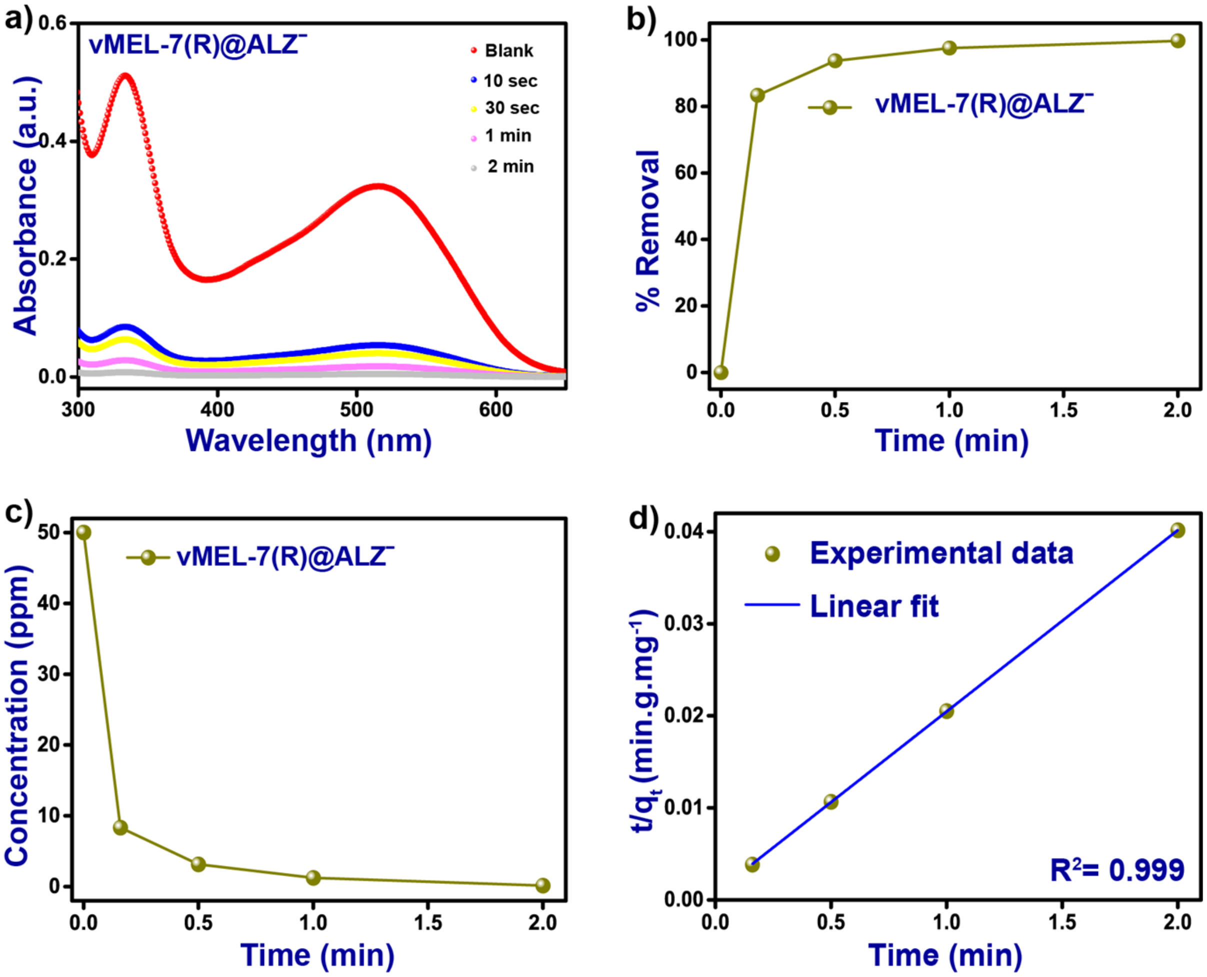

Figure S29: Capture study of Alizarin red S (ARS^-) via vMEL-7(R): a) UV-vis spectra of ARS^- show diminishing in the absorbance with increasing time, b) % removal vs time, c) Decrease in the concentration with time, d) Pseudo-second-order model fitting for ARS^- capture.

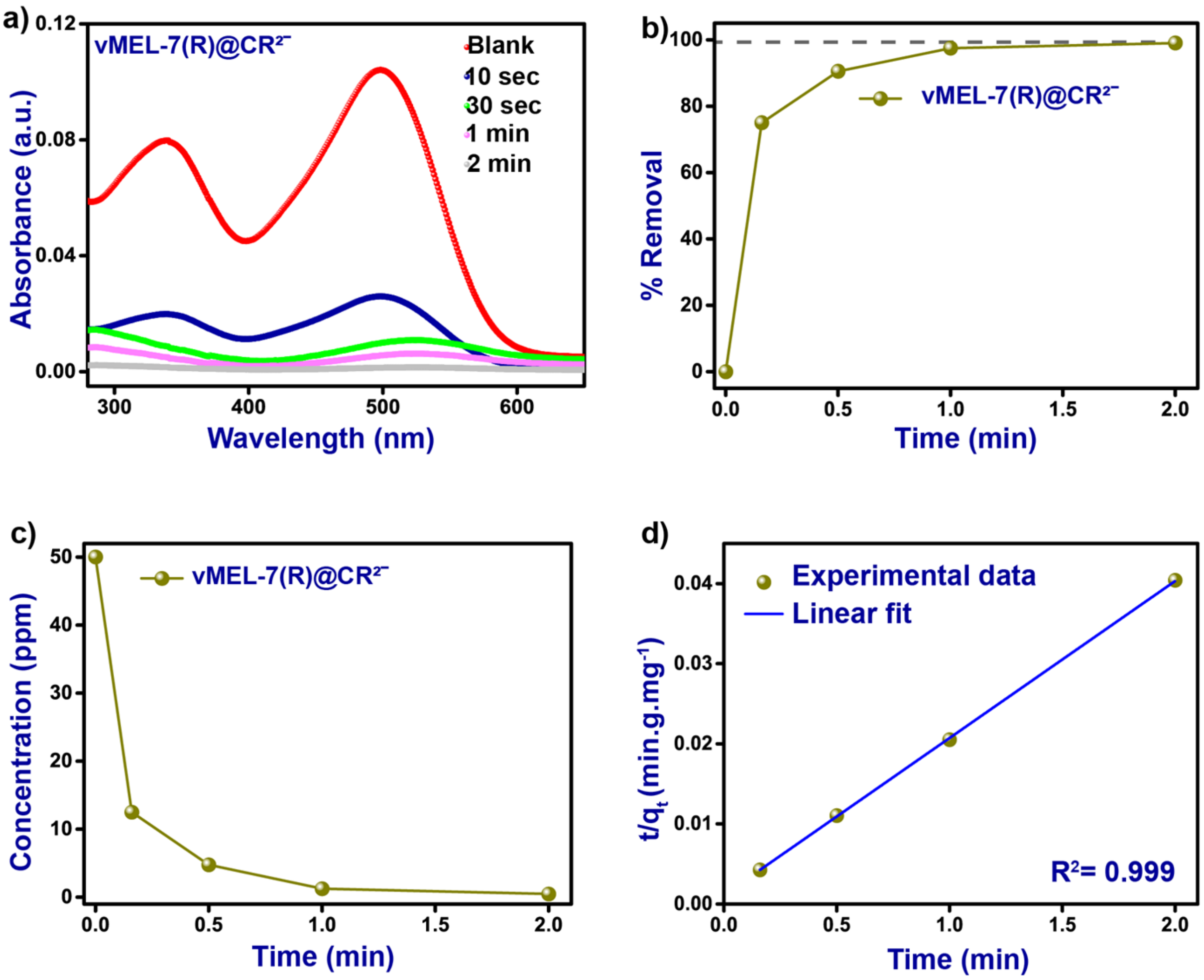

Figure S30: Capture study of Congo red (CR^{2-}) via vMEL-7(R): a) UV-vis spectra of CR^{2-} show diminishing in the absorbance with increasing time, b) % removal vs time, c) Decrease in the concentration with time, d) Pseudo-second-order model fitting for CR^{2-} capture.

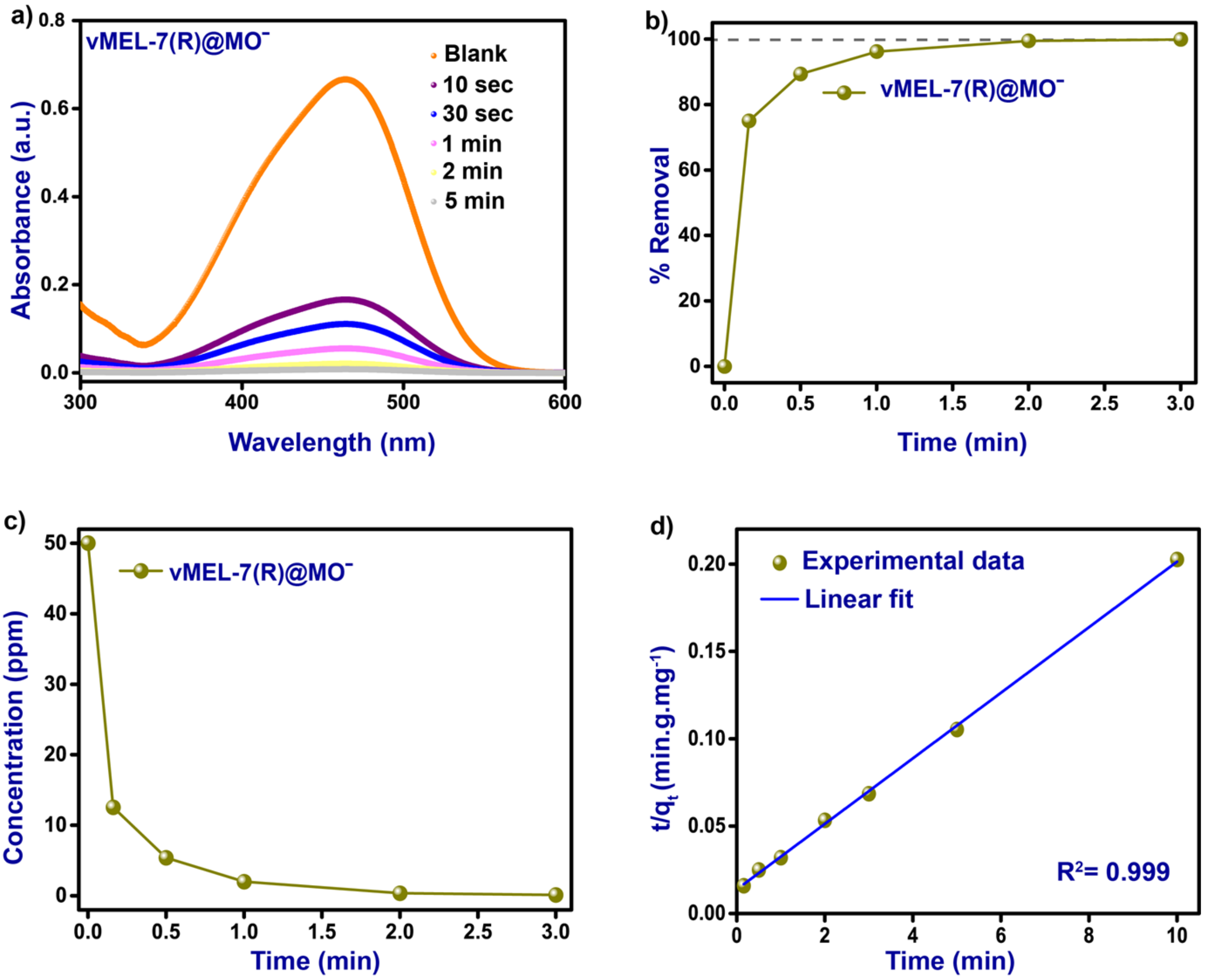

Figure S31: Capture study of Methyl orange (MO^-) via vMEL-7(R): a) UV-vis spectra of MO^- show diminishing in the absorbance with increasing time, b) % removal vs time, c) Decrease in the concentration with time, d) Pseudo-second-order model fitting for MO^- capture.

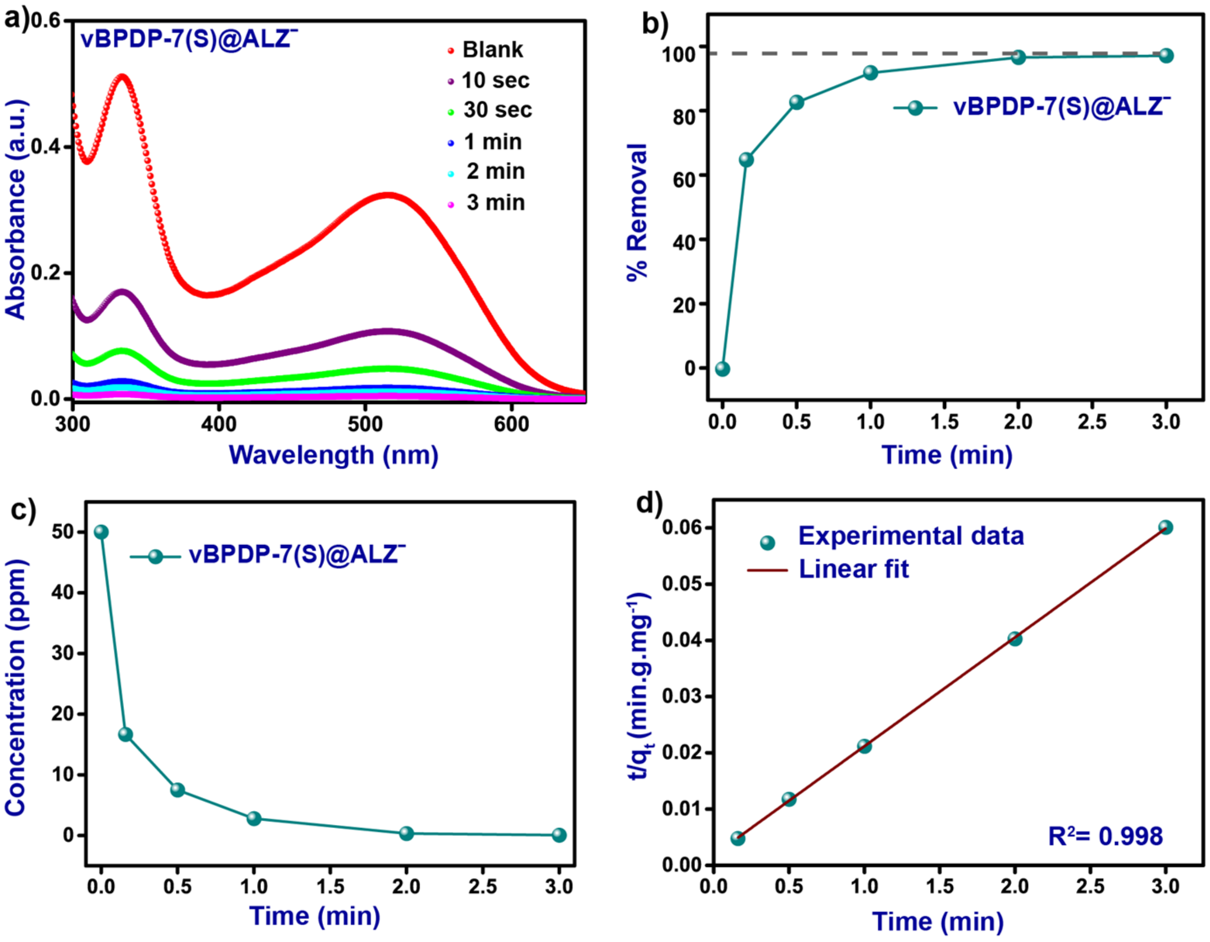

Figure S32: Capture study of Alizarin red S (ARS$^-$) via vBPDP-7(S): a) UV-vis spectra of ARS$^-$ show diminishing in the absorbance with increasing time, b) % removal vs time, c) Decrease in the concentration with time, d) Pseudo-second-order model fitting for ARS$^-$ capture.

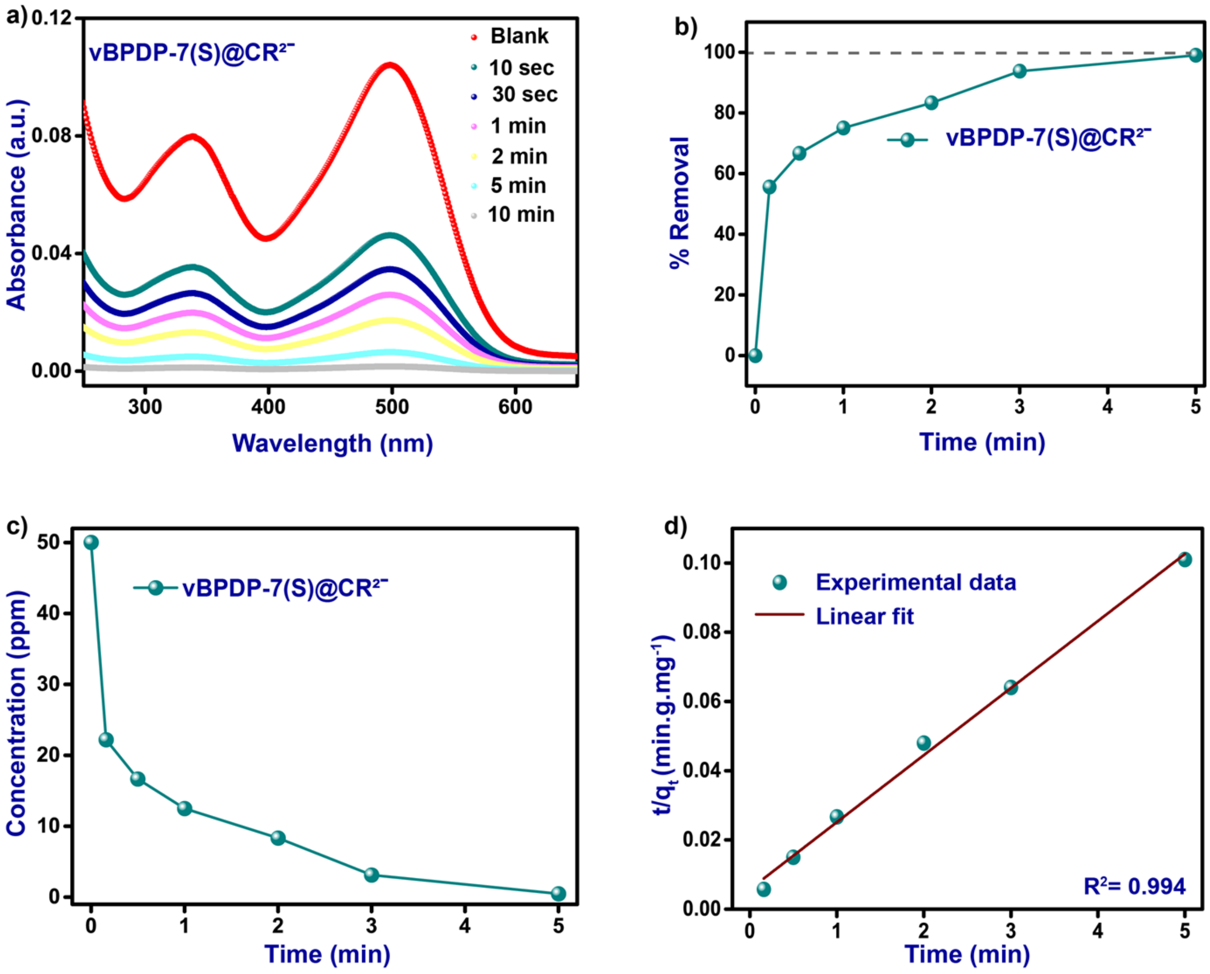

Figure S33: Capture study of Congo red (CR^{2-}) via vBPDP-7(S): a) UV-vis spectra of CR^{2-} show diminishing in the absorbance with increasing time, b) % removal vs time, c) Decrease in the concentration with time, d) Pseudo-second-order model fitting for CR^{2-} capture.

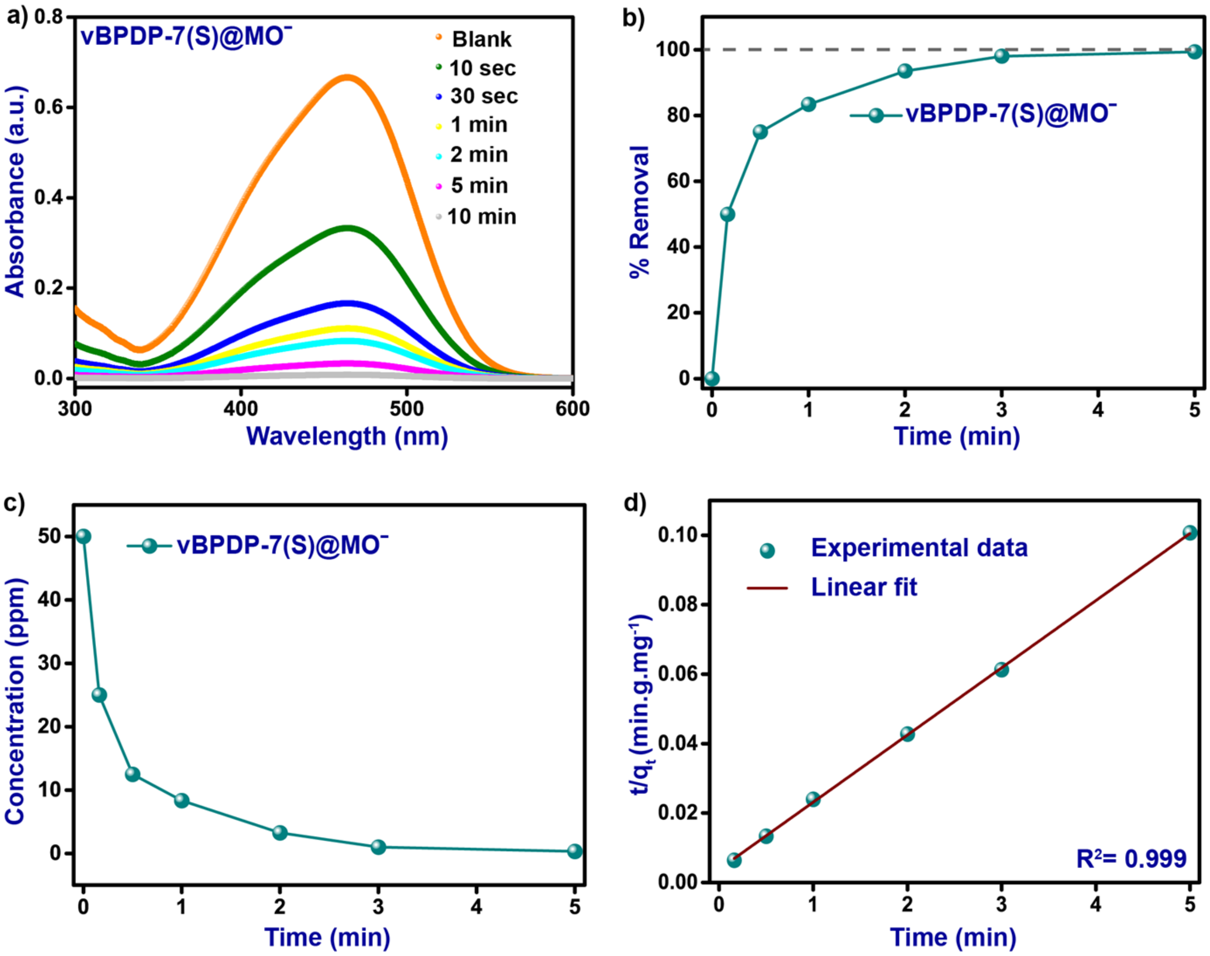

Figure S34: Capture study of Methyl orange (MO^-) via vBPDP-7(S): a) UV-vis spectra of MO^- show diminishing in the absorbance with increasing time, b) % removal vs time, c) Decrease in the concentration with time, d) Pseudo-second-order model fitting for MO^- capture.

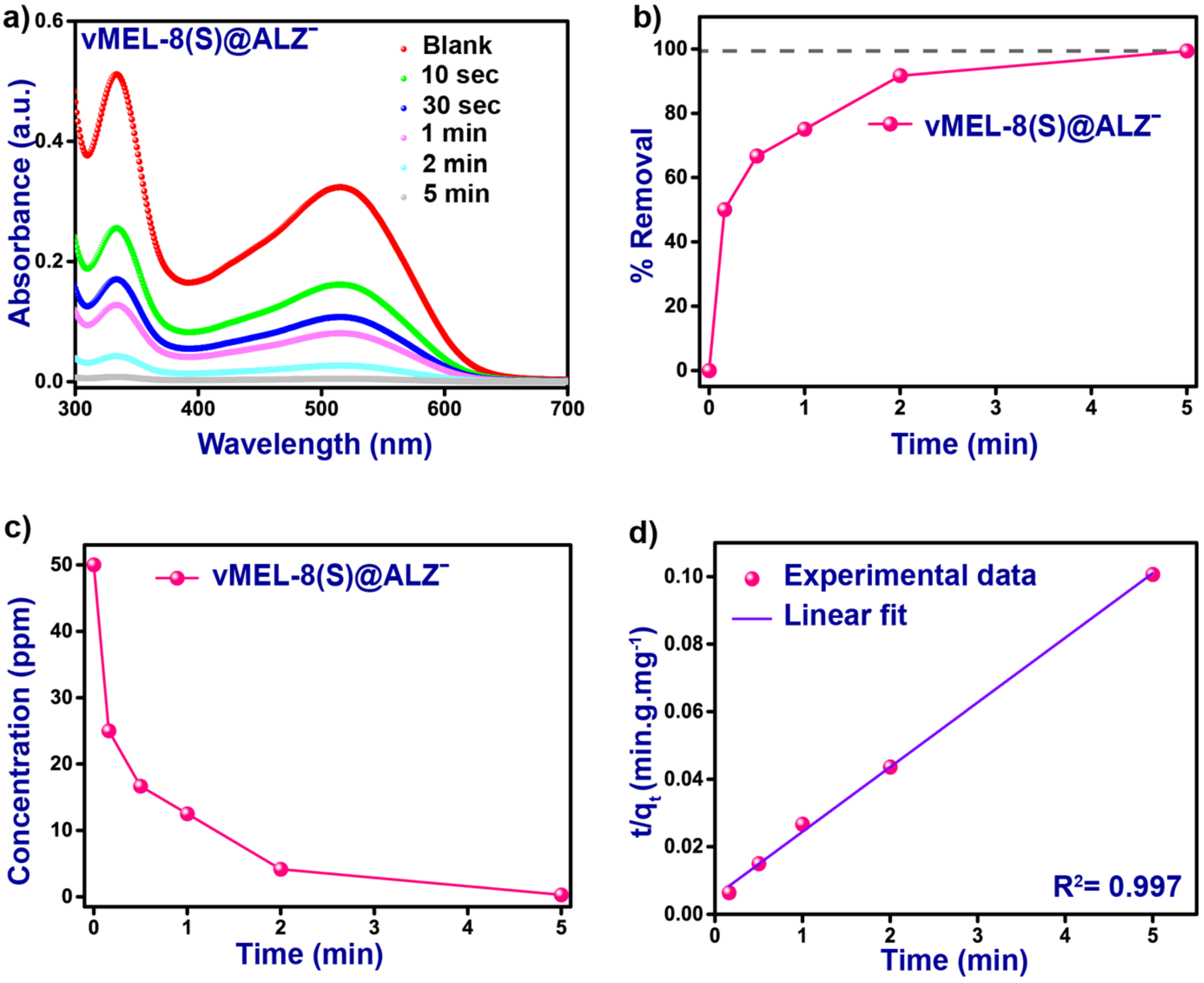

Figure S35: Capture study of Alizarin red S (ARS$^-$) via vMEL-8(S): a) UV-vis spectra of ARS$^-$ show diminishing in the absorbance with increasing time, b) % removal vs time, c) Decrease in the concentration with time, d) Pseudo-second-order model fitting for ARS$^-$ capture.

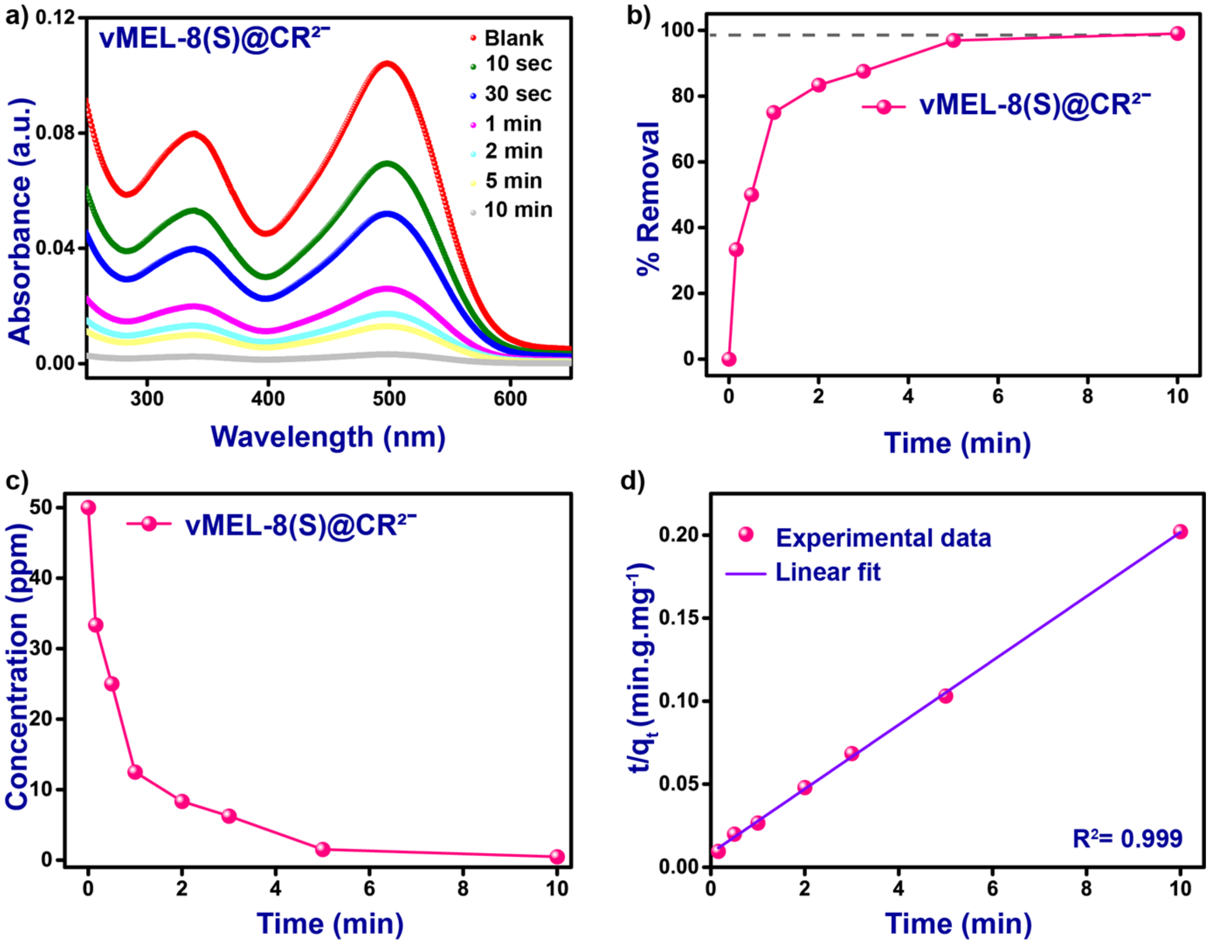

Figure S36: Capture study of Congo red (CR^{2-}) via vMEL-8(S): a) UV-vis spectra of CR^{2-} show diminishing in the absorbance with increasing time, b) % removal vs time, c) Decrease in the concentration with time, d) Pseudo-second-order model fitting for CR^{2-} capture.

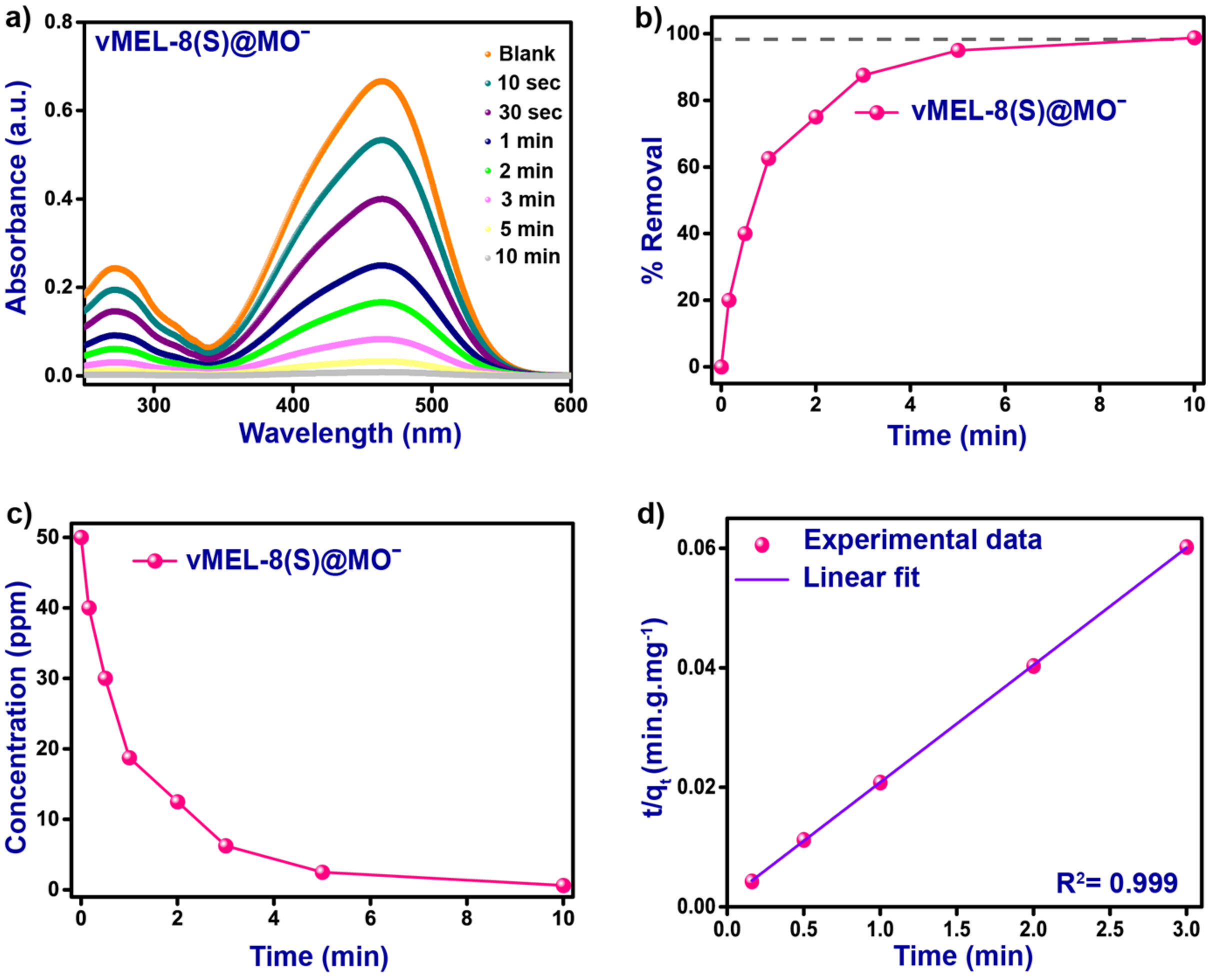

Figure S37: Capture study of Methyl orange (MO^-) via vMEL-8(s): a) UV-vis spectra of MO^- show diminishing in the absorbance with increasing time, b) % removal vs time, c) Decrease in the concentration with time, d) Pseudo-second-order model fitting for MO^- capture.

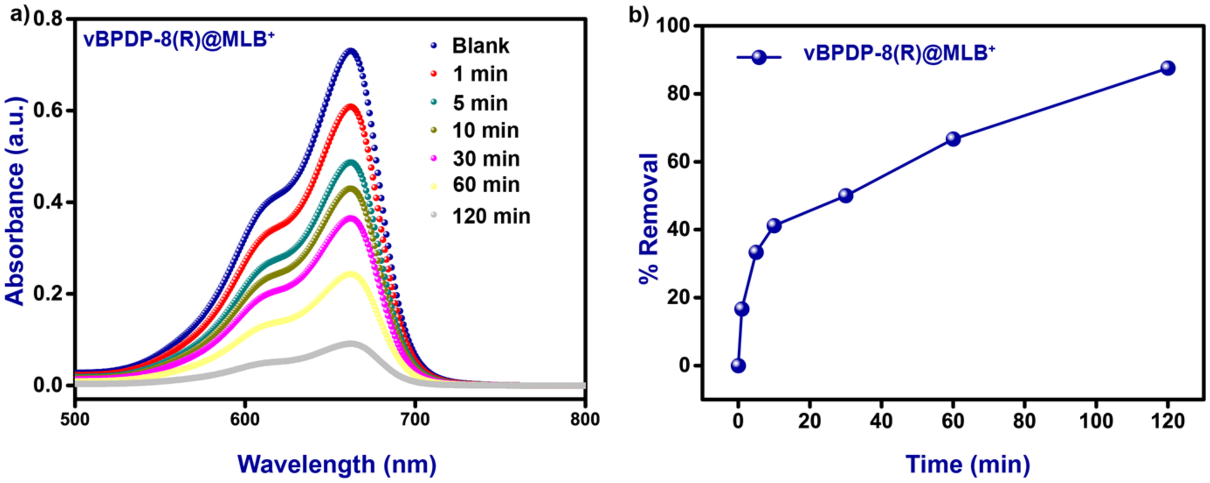

Figure S38: Capture study of Methylene blue (MLB$^+$) via vBPDP-8(R): a) UV-vis spectra of MLB$^+$ shows diminishing in the absorbance with increasing time, b) % removal vs time.

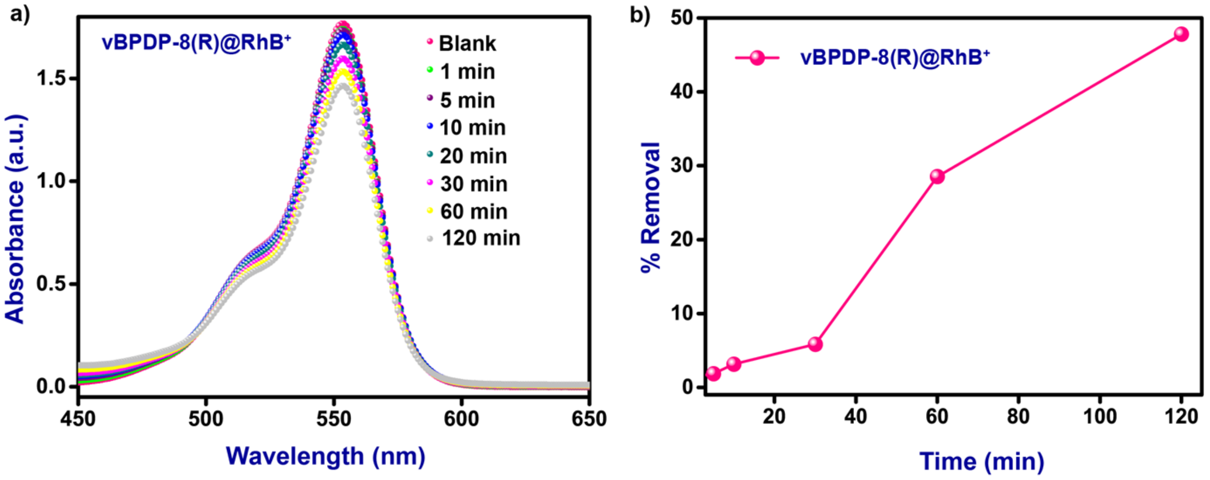

Figure S39: Capture study of Rhodium B (RhB$^+$) via vBPDP-8(R): a) UV-vis spectra of RhB$^+$ shows diminishing in the absorbance with increasing time, b) % removal vs time.

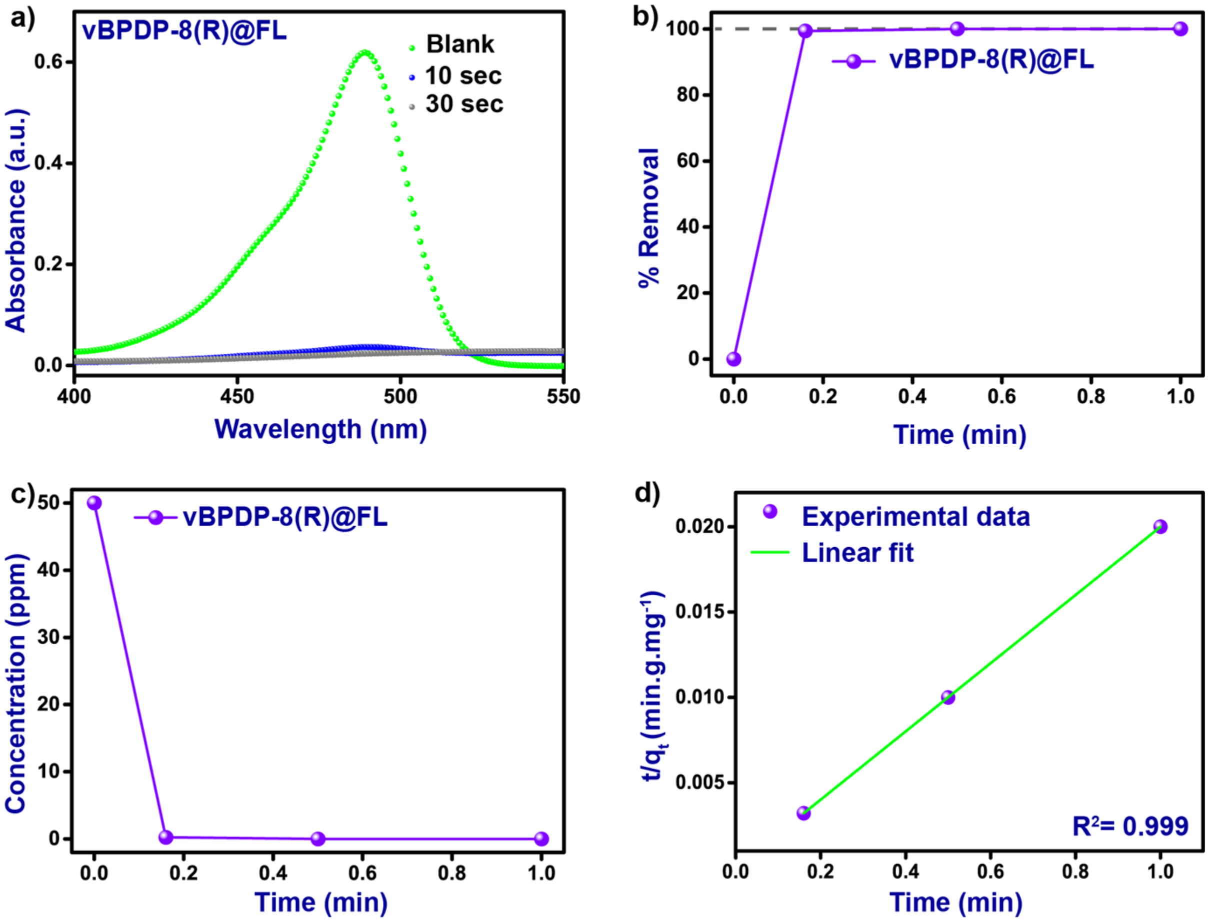

Figure S40: Capture study of Fluorescein (FL) via vBPDP-8(R): a) UV-vis spectra of FL shows diminishing in the absorbance with increasing time, b) % removal vs time, c) Decrease in the concentration with time, d) Pseudo-second-order model fitting for FL capture.

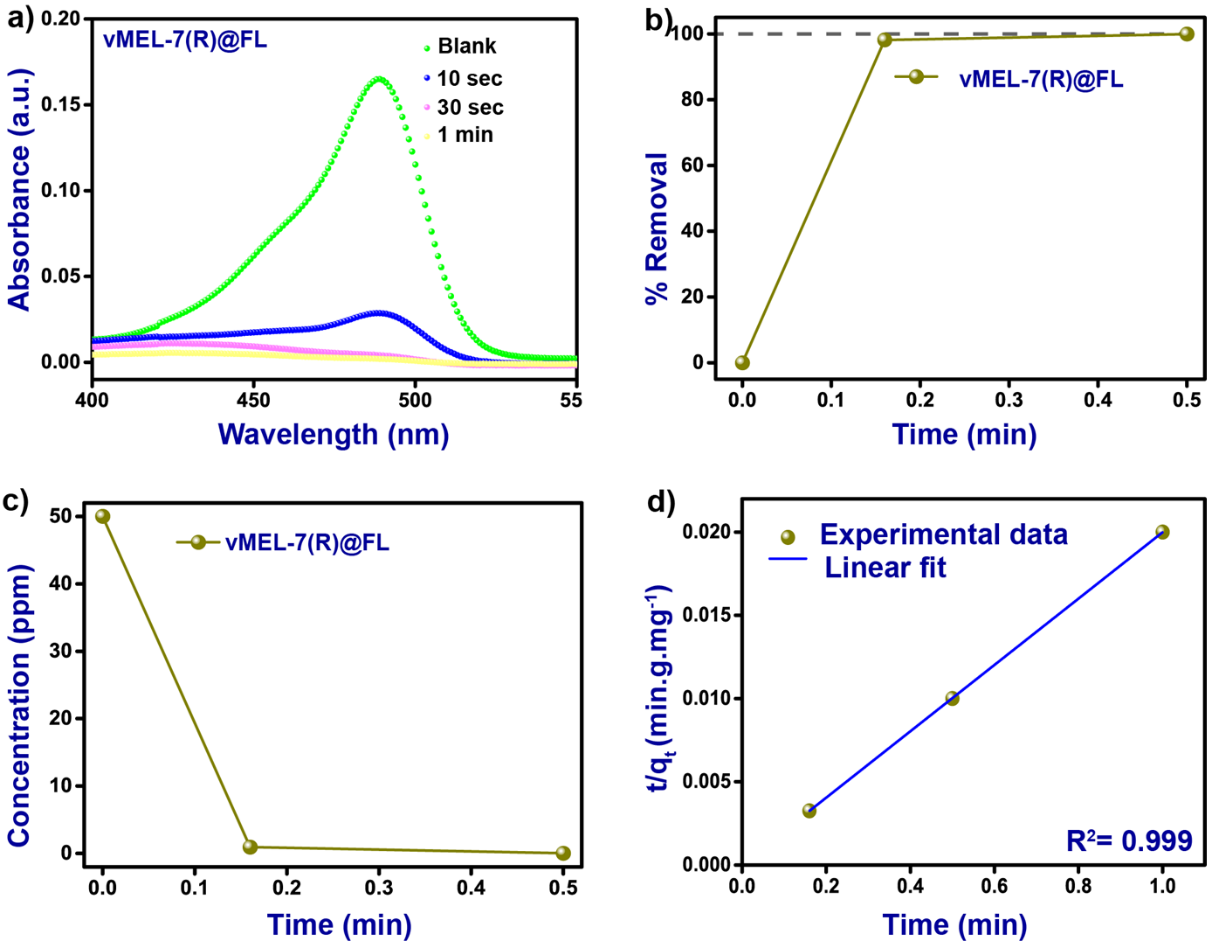

Figure S41: Capture study of Fluorescein (FL) via vMEL-7(R): a) UV-vis spectra of FL shows diminishing in the absorbance with increasing time, b) % removal vs time, c) Decrease in the concentration with time, d) Pseudo-second-order model fitting for FL capture.

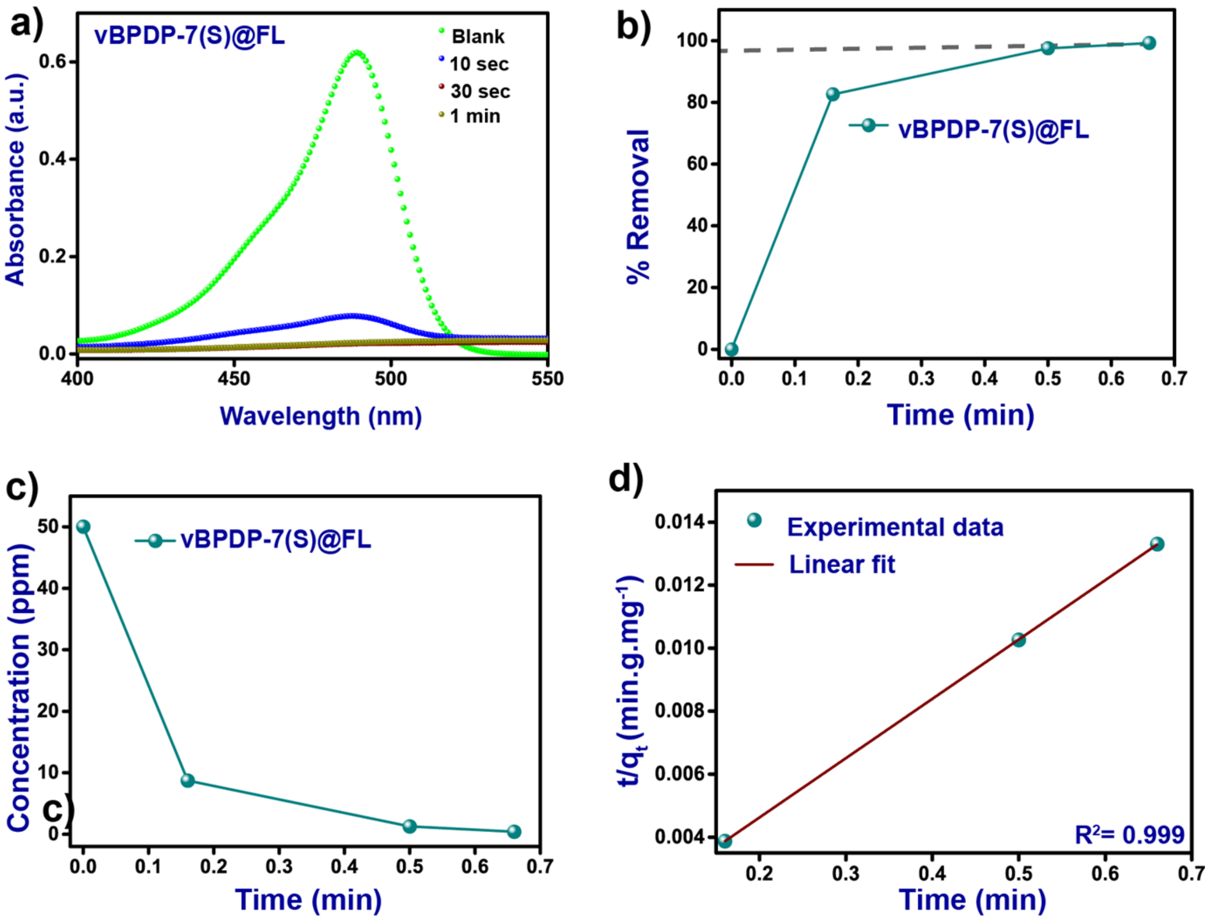

Figure S42: Capture study of Fluorescein (FL) via vBPDP-7(S): a) UV-vis spectra of FL shows diminishing in the absorbance with increasing time, b) % removal vs time, c) Decrease in the concentration with time, d) Pseudo-second-order model fitting for FL capture.

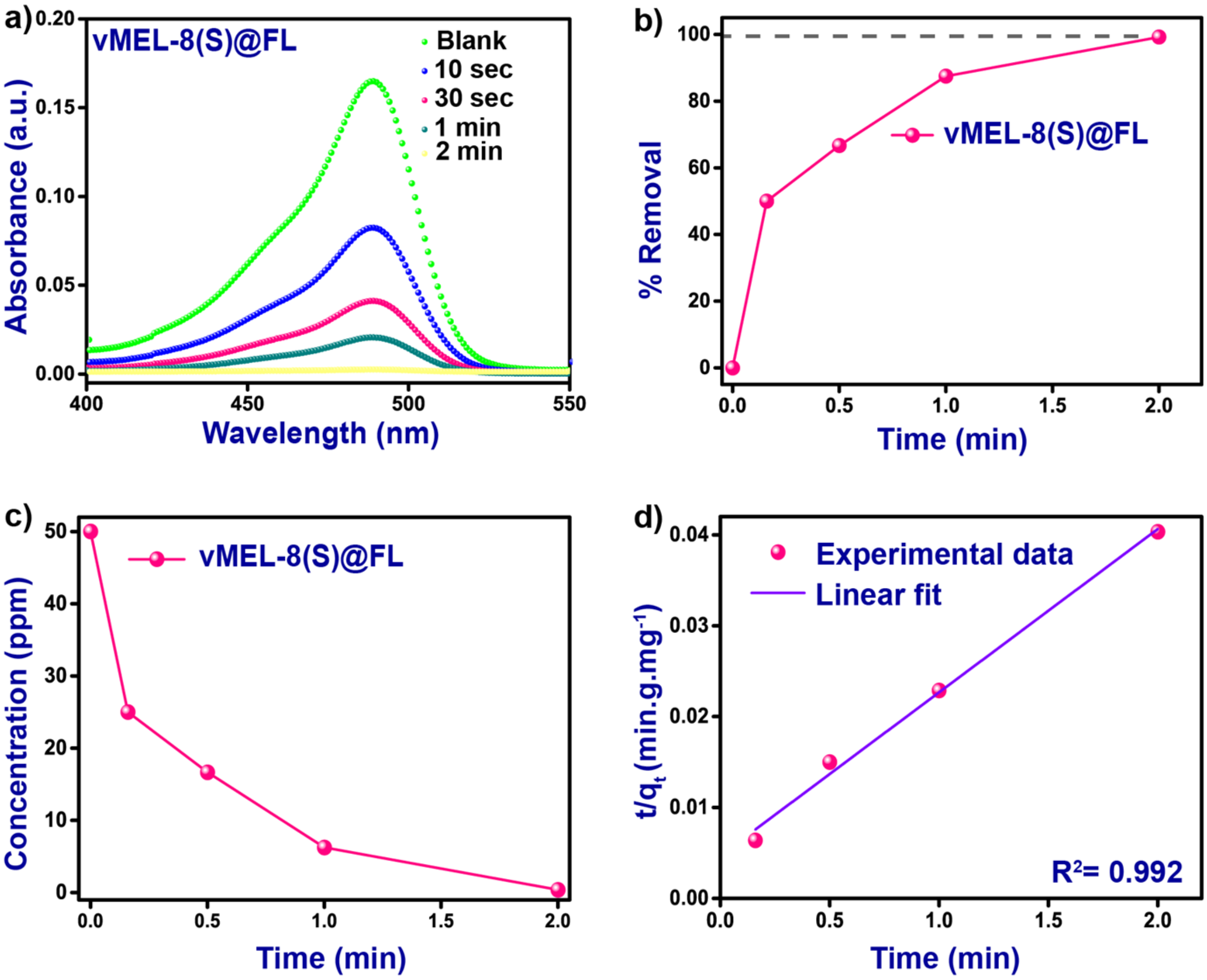

Figure S43: Capture study of Fluorescein (FL) via vMEL-8(S): a) UV-vis spectra of FL shows diminishing in the absorbance with increasing time, b) % removal vs time, c) Decrease in the concentration with time, d) Pseudo-second-order model fitting for FL capture.

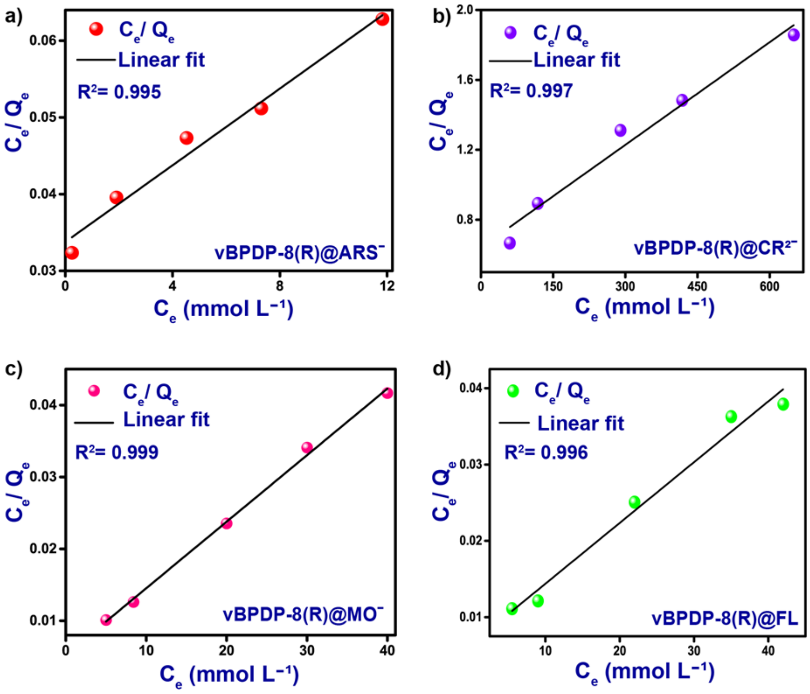

Figure S44: Langmuir model of a) ARS⁻, b) CR²⁻, c) MO⁻ and d) FL capture through vBPDP-8(R).

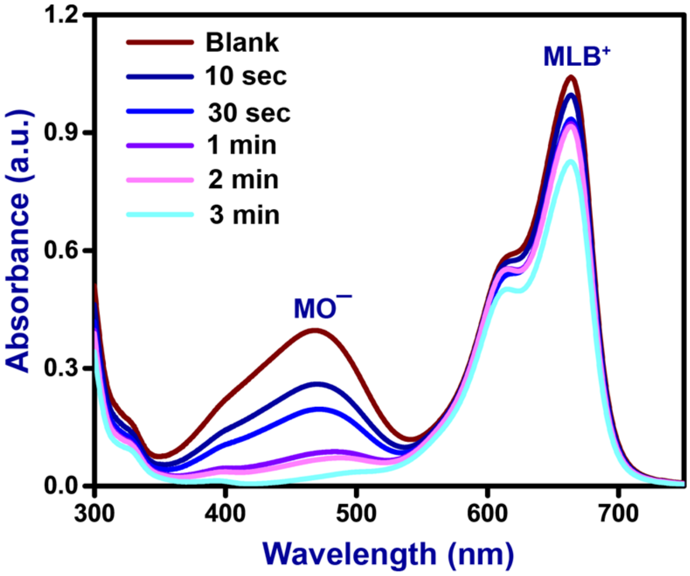

Figure S45: Capture study of the mixed MO and MLB dyes solution via vBPDP-8(R) for the charge-dependent selective separation.

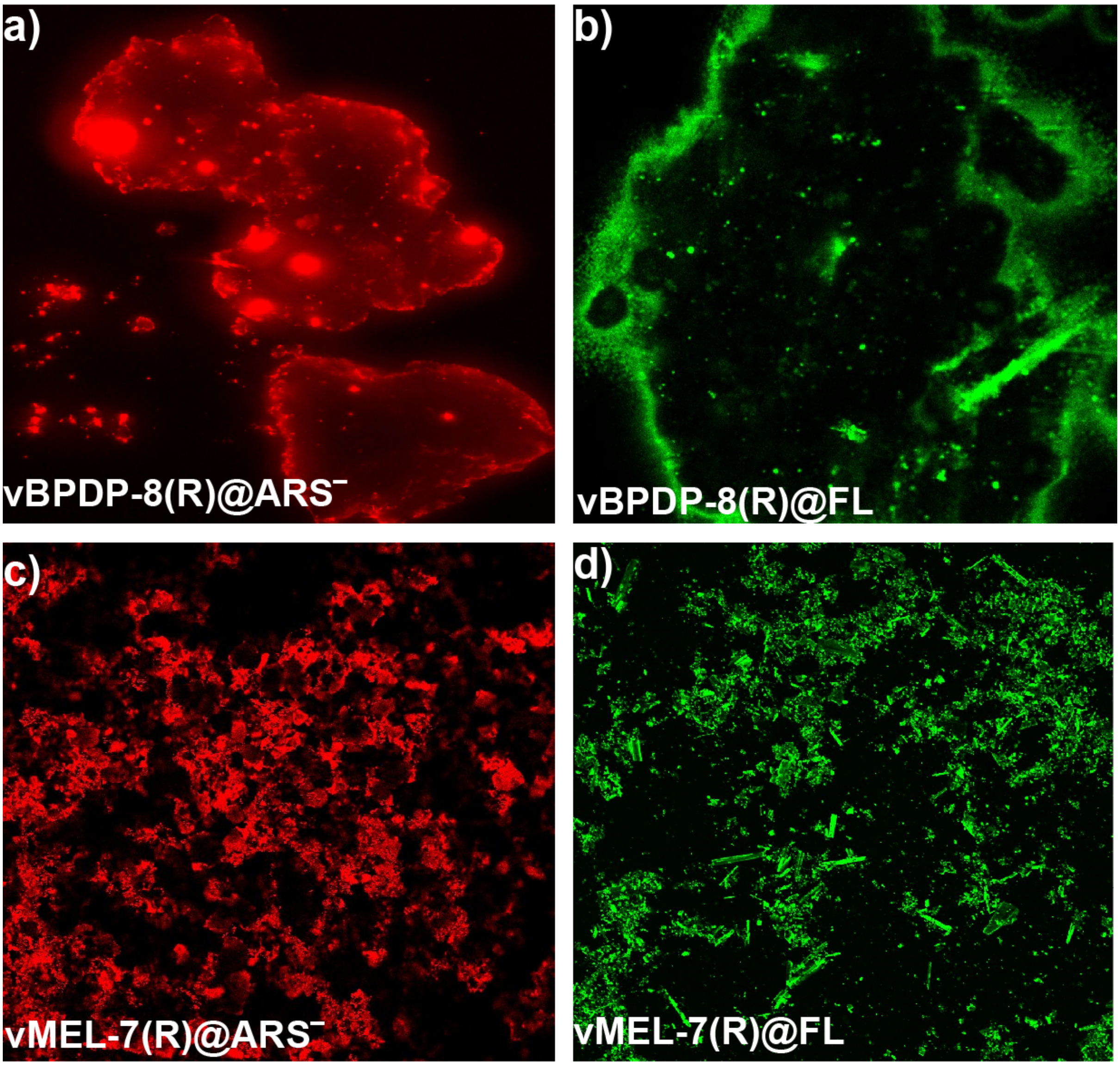

Figure S46: Confocal images of a) vBPDP-8(R)@ARS⁻, b) vBPDP-8(R)@FL, c) vMEL-7(R)@ARS⁻, and d) vMEL-7(R)@FL. The confocal images of vBPDP-8(R) and vMEL-7(R) shows the adsorption of dyes in the peripheral and surface regions.

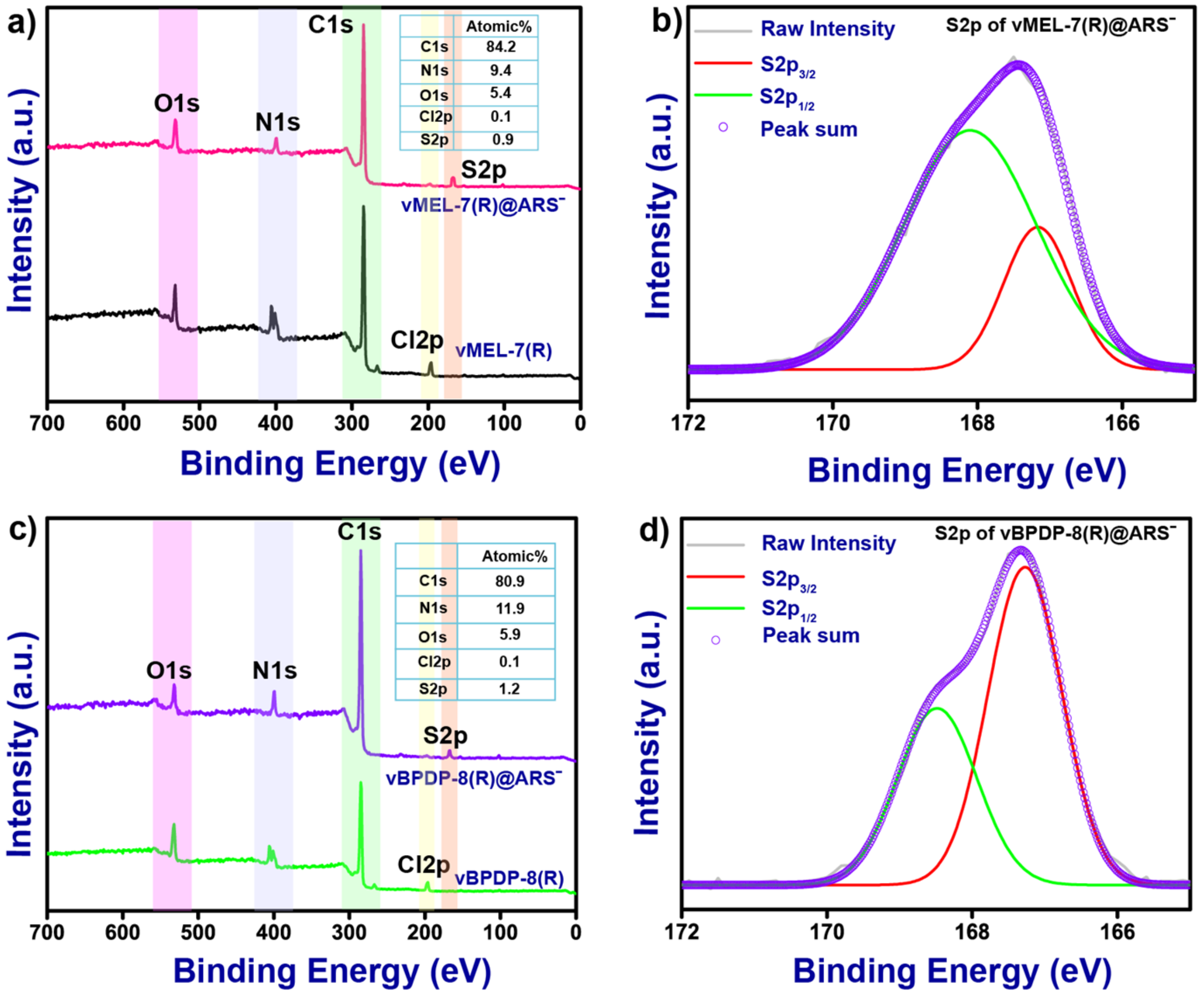

	Atomic%
C1s	84.2
N1s	9.4
O1s	5.4
Cl2p	0.1
S2p	0.9

	Atomic%
C1s	80.9
N1s	11.9
O1s	5.9
Cl2p	0.1
S2p	1.2

Figure S47: XPS survey scan of a) vBDPD-8(R)@ARS⁻ and c) vMEL-7(R)@ARS⁻. Deconvoluted S2p orbital of b) vBDPD-8(R)@ARS⁻ and d) vMEL-7(R)@ARS⁻.

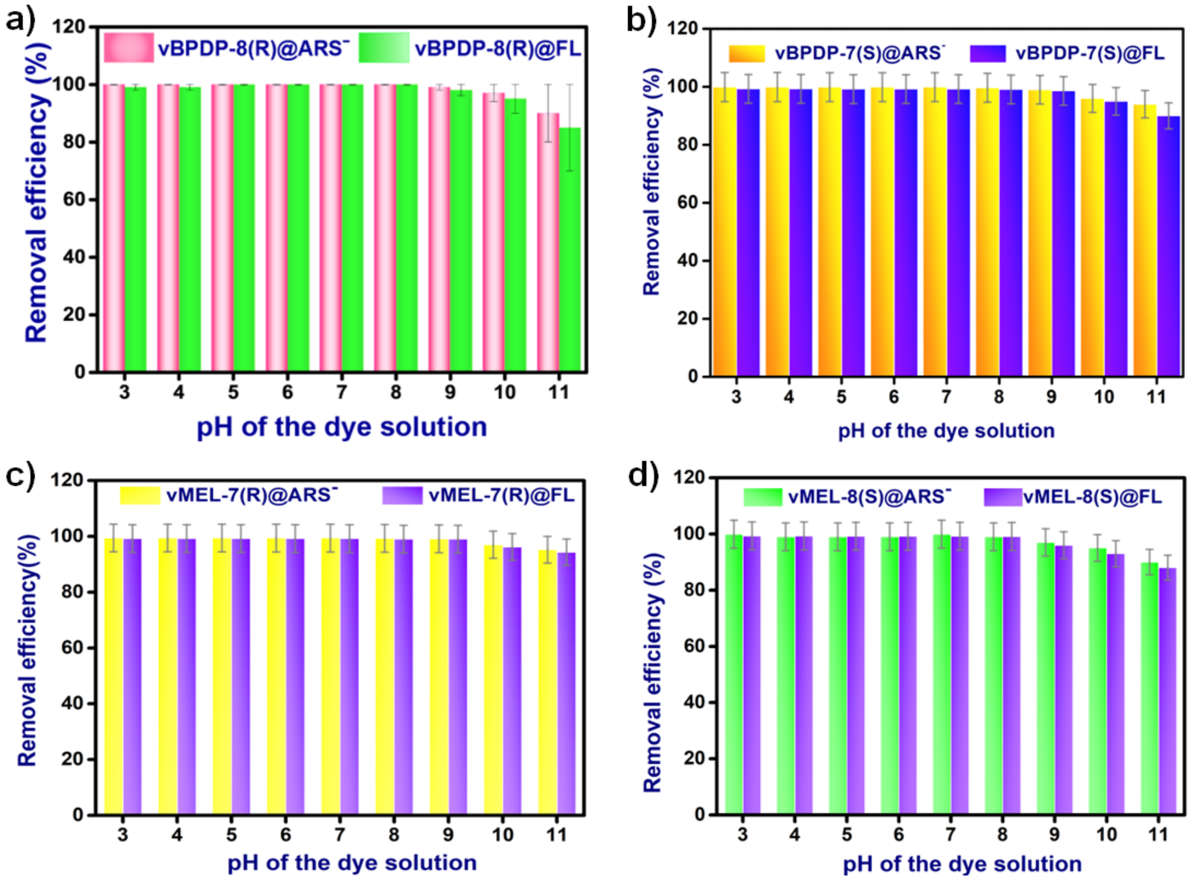

Figure S48: Removal efficiency of ARS⁻ and FL with vBPDP-8(R) and vMEL-7(R) at different pH values (3 to 11).

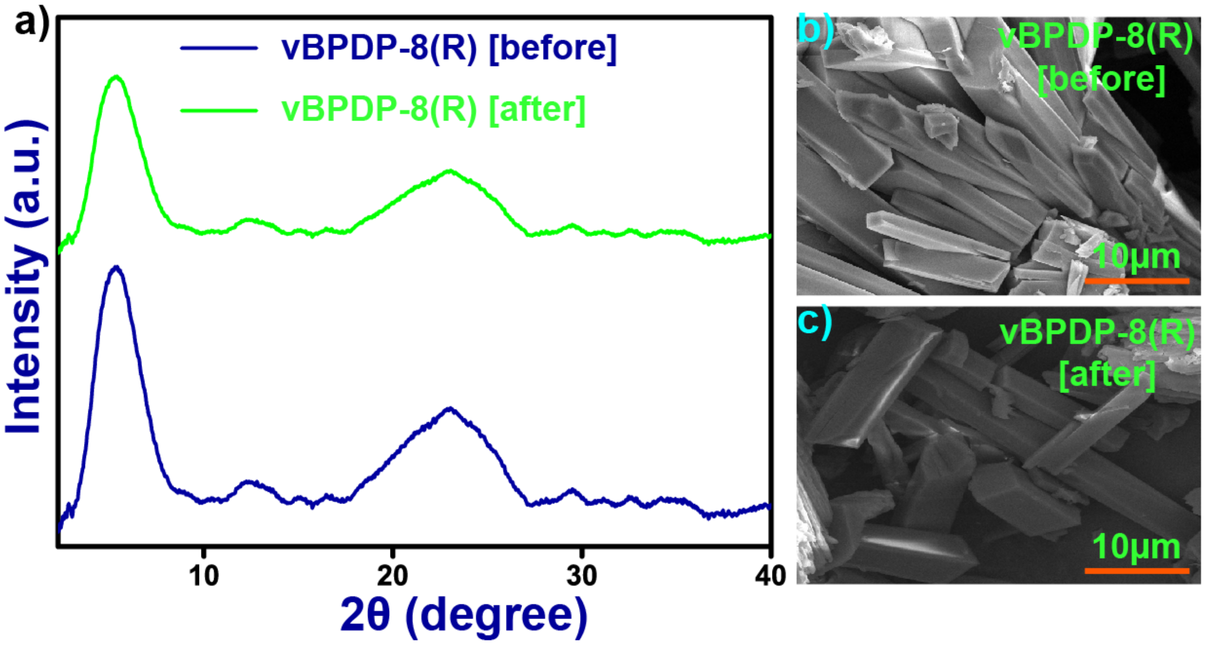

Figure S49: a) Powder pattern of vBPDP-8(R) before and after FL capture experiment. FESEM micrographs of vBPDP-8(R) to compare its morphology b) before and c) after FL capture experiment. Even after the experiment, the framework managed to maintain their rod-shaped morphology.

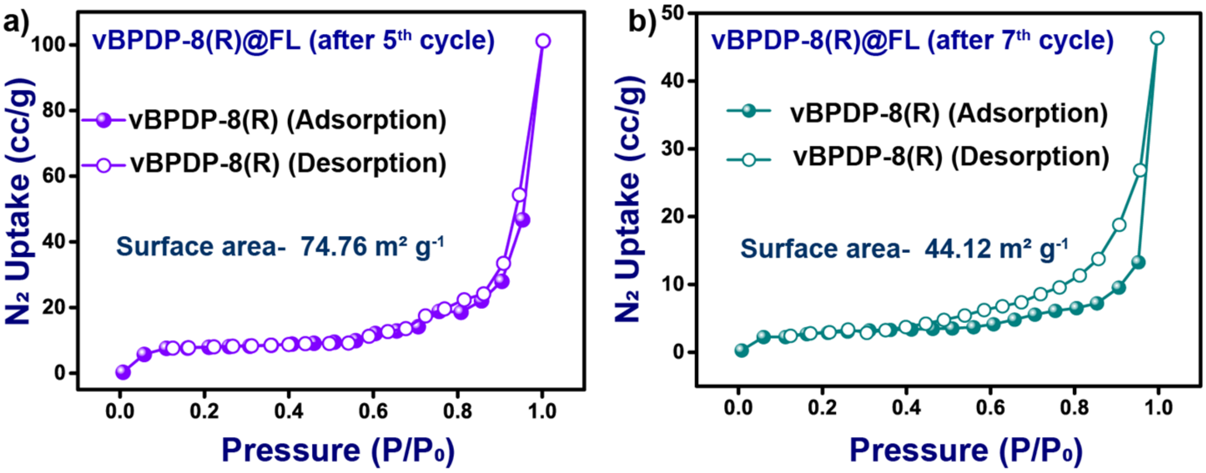

Figure S50: N_2 sorption isotherm curves and BET surface area analysis of a) vBPDP-8(R)@FL after 5th cycle, and b) vBPDP-8(R)@FL after 7th cycle.

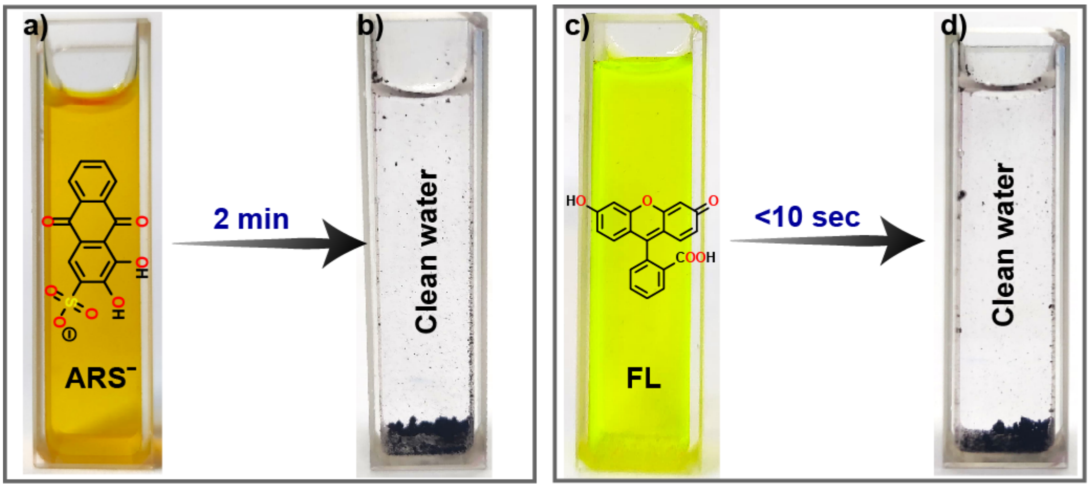

Figure S51: a-b) The real photographs show the colors of aqueous solutions of ARS⁻ before and after the (arrow) filtration process, respectively, c-d) a-b) The real photographs show the colors of aqueous solutions of FL before and after the (arrow) filtration process.

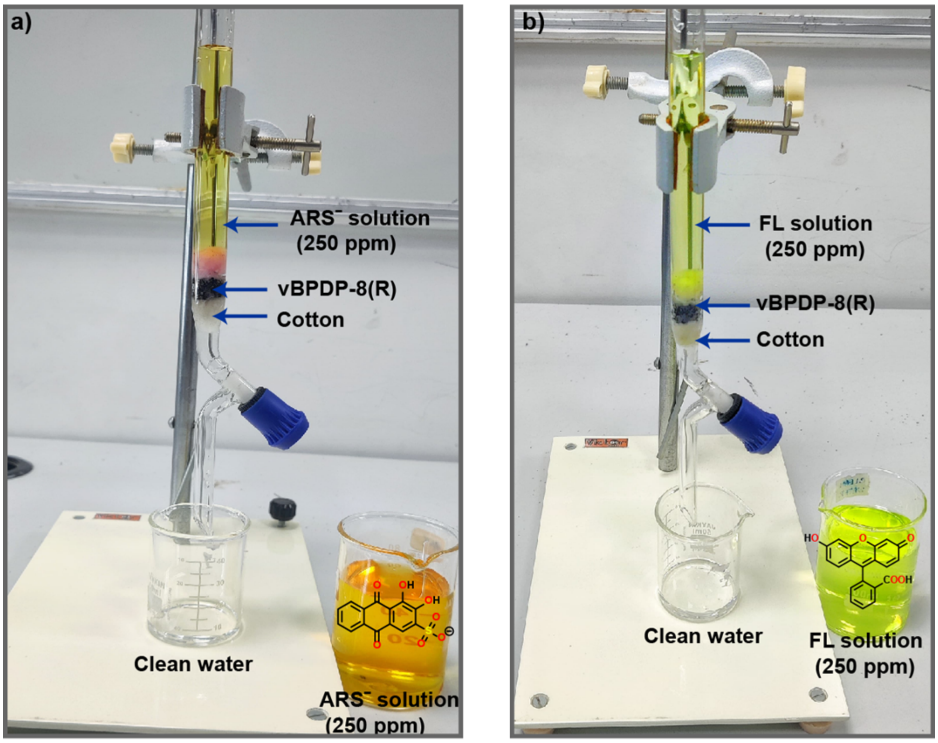

Figure S52: a-b) Pollutant (ARS⁻ and FL) removal efficiency measured through a column bed of vBPDP-8(R).

SVI: Density Functional Theory:

We performed DFT studies to further investigate the selective and rapid sequestration, aiming to gain a deeper understanding of the experimental findings. The DFT simulation was performed with a focus on a single polymeric network. The interactions at the molecular scale between vBPDP and vMEL and the dyes (anionic- ARS⁻, cationic- MB⁺ and neutral- FL dyes we chose for the DFT studies) were examined with Gaussian 16.0 software.

The binding energy was then calculated using equation 1 (eq1.)

$\Delta E = E_{COF + ion} - E_{COF} - E_{ion}$……….$eq1.$

QTAIM analysis:

Quantum Theory of Atoms in Molecules (QTAIM) provides a detailed, atomic level understanding of the COF–dye interactions by analysing intermolecular contacts. Within this framework, each functional atom in the COF is defined by its local electron density and hessian curvature, which collectively differentiate pure electrostatic attraction from covalent bond or π-stacking anisotropy. Through the mapping of bond critical points(BCPs) and the quantification of descriptors such as the electron density [ρ(r)], the Laplacian of electron density [$\nabla^2\rho(r)$], the eigenvalues of the Hessian matrix (λ_1 and λ_2), the ellipticity (ε), the potential energy density [V(r)], the Lagrangian kinetic energy [G(r)], and the electronic energy density [H(r)] QTAIM accurately identifies the precise locations of dye anchoring while elucidating the intrinsic characteristics and comparative strength of each interaction, which gives rise to the explanation behind improved dye capture.

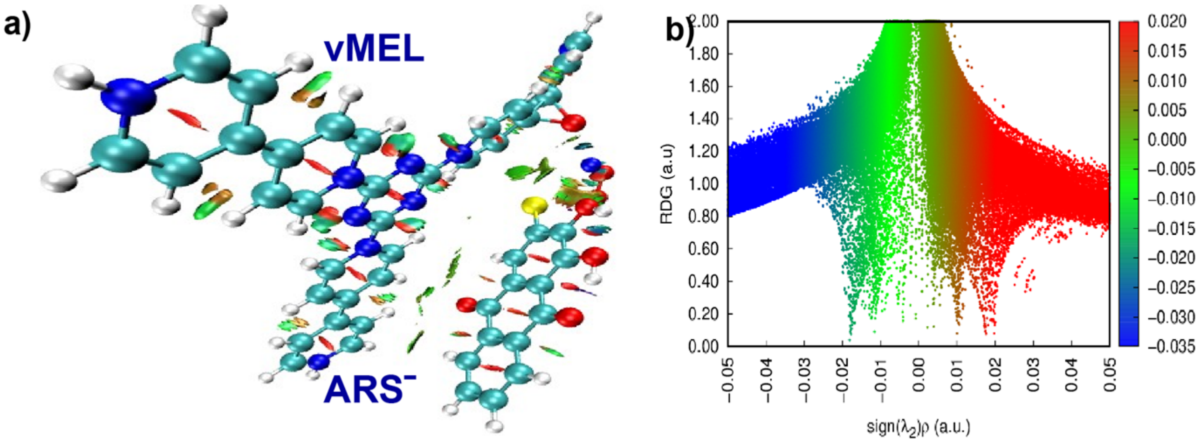

Figure S53: a) Molecular-level interaction between vMEL with Alizarin red S (ARS⁻, anionic dye), b) Reduced density gradient (RDG) plots of vMEL interacted with ARS⁻.

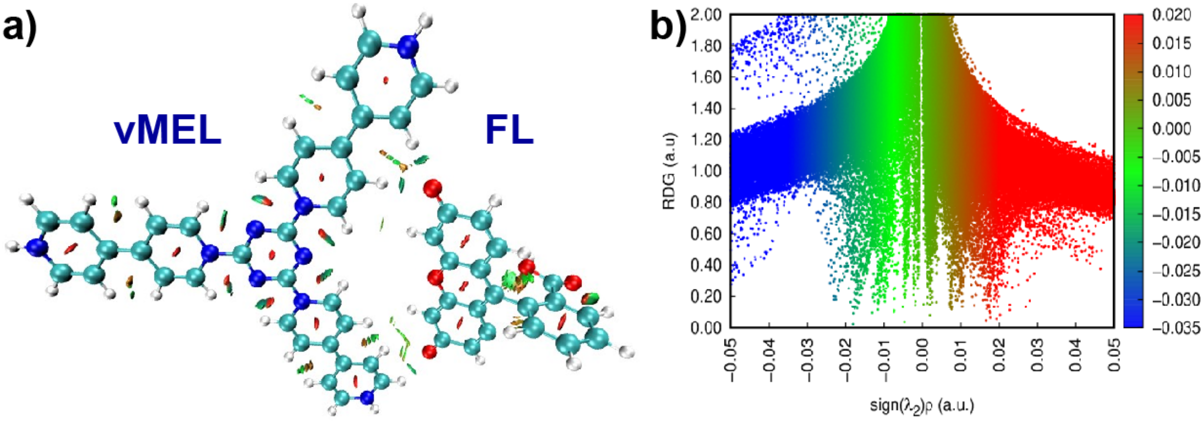

Figure S54: a) Molecular-level interaction between vMEL with Fluoresceine (FL, neutral dye), b) Reduced density gradient (RDG) plots of vMEL interacted with FL.

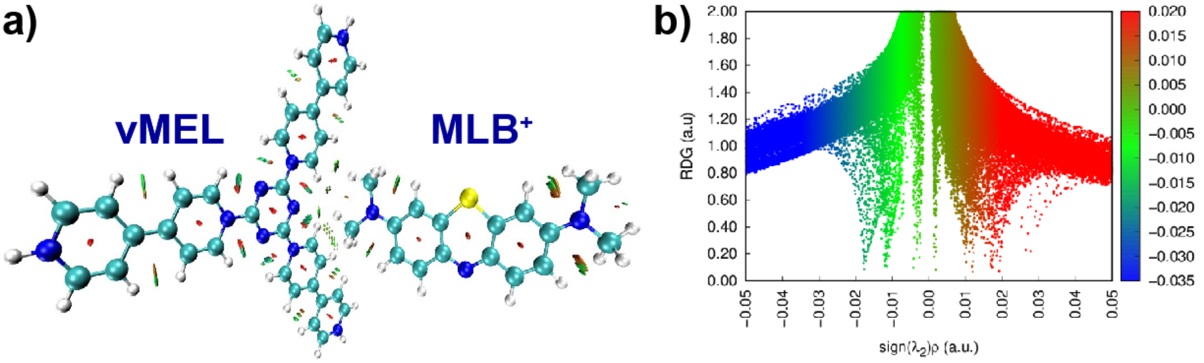

Figure S55: a) Molecular-level interaction between vMEL with Methylene blue (MLB^+, cationic dye), b) Reduced density gradient (RDG) plots of vMEL interacted with MLB^+.

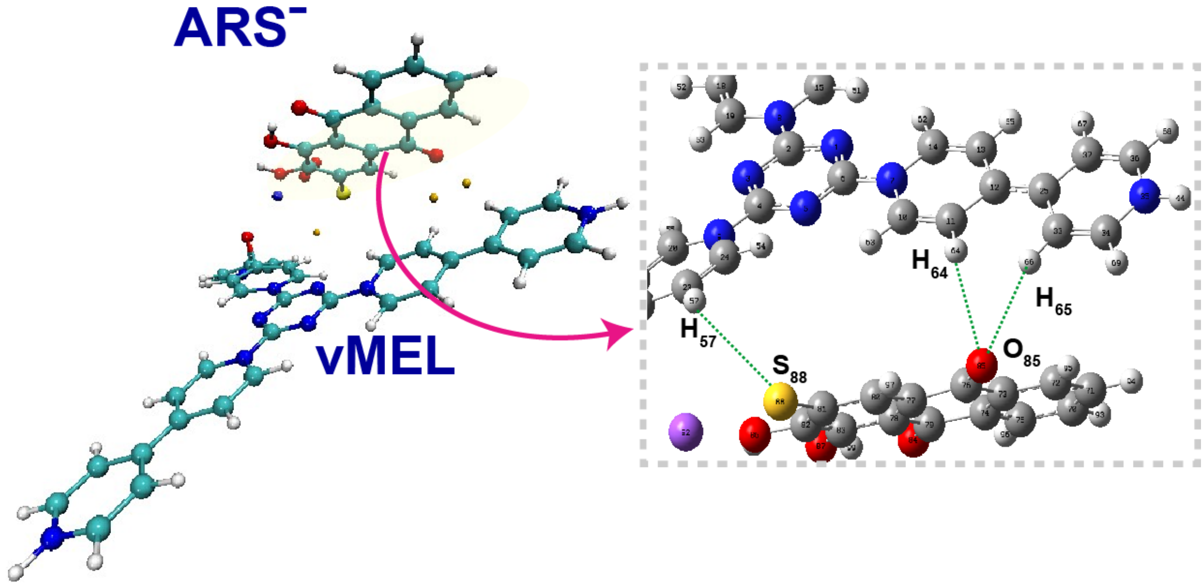

Figure S56: QTAIM-mapped bond critical points between the vMEL and ARS^-.

vBPDP@ARS^- exhibits four bond critical points (BCPs) versus two for vBPDP@FL, reflecting a more intricate interaction network (Fig. 5k- 5l). In case of ARS^-, the electron density ρ(r) spans 0.0025–0.0119 a.u., whereas FL showed contacts range from 0.0166–0.0456 a.u., indicating multiple moderate hydrogen bonds rather than isolated strong contacts. The ellipticity ε (λ_1/λ_2 – 1) of vBPDP@ARS^- is nearly zero, consistent with symmetric σ-type H-bonds, while vBPDP@FL displays pronounced ε values, denoting anisotropy. Although the potential energy densities V(r) (–0.0014 to –0.0128 a.u.) of vBPDP@ARS^- are individually less negative than vBPDP@FL (–0.0117 to –0.0355 a.u.), the average over four sites yields comparable stabilization (Table S8). Furthermore, the summed total energy densities H(r) for vBPDP@ARS^- ~ 0.0009, 0.0009, 0.0028, and 0.0054 a.u., averaging about 0.0025 a.u., substantially surpass those of vBPDP@FL (–0.0007 and 0.0000 a.u., total ≈ 0.0007 a.u.), indicating that vBPDP binds ARS^- significantly more strongly.

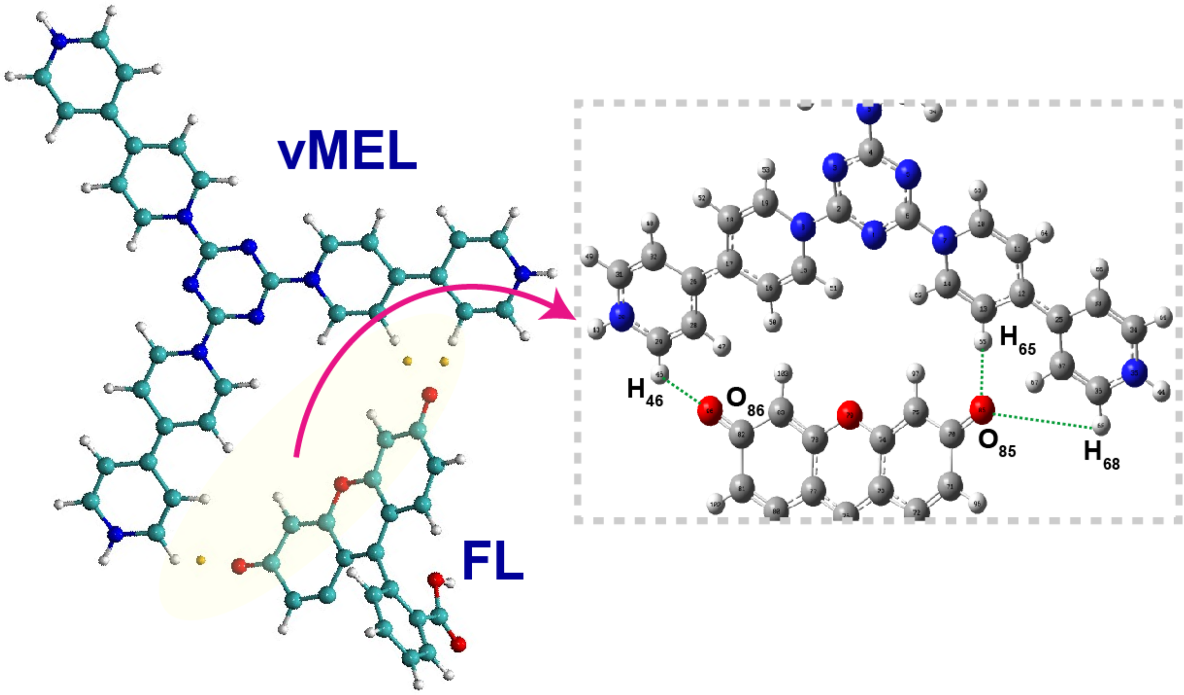

Figure S57: QTAIM-mapped bond critical points between the vMEL and FL.

vMEL@ARS$^-$ establishes three equivalent (Fig. S56, video S5), closed-shell hydrogen bonds—with ρ(r) between 0.0071 and 0.0082 a.u., $\nabla^2\rho(r)$ from 0.0365 to 0.0473 a.u., and ellipticities of roughly 0.03–0.07—that each exhibit positive total energy densities (H(r) = 0.0006–0.0008 a.u.; ΣH ≈ 0.0021 a.u.).In contrast, the three bond critical points of vMEL@FL (Fig. S57)exhibit a broader electron-density range (ρ(r) = 0.0041–0.0095 a.u.) and higher ellipticity values, culminating in an essentially zero cumulative total energy density (∑H(r) ≈ 0.0001 a.u.), thereby confirming that Alizarin associates with VMEL more favorably than fluorescein.

SVII: Supporting Table:

Table S1. Various combinations of solvent mixture for the synthesis of vBPDP and vMEL with morphological diversity:

Sl. no	Reaction conditions	Solvent mixture	Product		Nature		Morphology	
			vBPDP	vMEL	vBPDP	vMEL	vBPDP	vMEL
1	120°C, 72 h	Ethanol/ water (4:1)	vBPDP-1	vMEL-1	amorphous	crystalline	Spherical	Rod-shaped
2	120°C, 72 h	Ethanol/ Cl-benzene/ 1,4-dioxane (1:1:1)	vBPDP-2	vMEL-2	Semi-crystalline	amorphous	Spherical	Aggregated
3	120°C, 72 h	Mesitylene/ 1,4-dioxane (1:1)	vBPDP-3	vMEL-3	amorphous	amorphous	Spherical	Rod-shaped
4	120°C, 72 h	o-dichlorobenzene+ DMSO (1:1)	vBPDP-4	vMEL-4	amorphous	amorphous	Aggregated	Aggregated
5	120°C, 72 h	1,4-dioxane/ ethanol (1:1)	vBPDP-5	vMEL-5	Not formed	amorphous	-------	Aggregated
6	120°C, 72 h	Ethanol/ mesitylene (1:1)	vBPDP-6	vMEL-6	Not formed	Not formed	------	-------
7	**120°C, 72 h**	**1,4-dioxane / water (2:1)**	**vBPDP-7**	**vMEL-7**	**crystalline**	**crystalline**	**Spherical**	**Rod-shaped**
8	**120°C, 72 h**	**Mesitylene/ water (4:1)**	**vBPDP-8**	**vMEL-8**	**crystalline**	**crystalline**	**Rod-shaped**	**Spherical**

Table S2. Q_{max} data of vCOFs:

Sample	Q_{max} (mg/g) of ALZ^{-}	Q_{max} (mg/g) of CR^{2-}	Q_{max} (mg/g) of MO^{-}	Q_{max} (mg/g) of FL
vBPDP-8(R)	**430.765547**	**457.7626542**	**1161.780734**	**1237.406098**
vMEL-7(R)	338.4689061	417.0565717	989.9482491	1024.083076
vBPDP-7(S)	257.8949169	291.0676308	798.6628558	863.8974812

vMEL-8(S)	210.1525621	204.1259039	764.5577081	795.5148034

Table S3. Q_{max} data of vBPDP-8(R) calculated through Langmuir Model:

Sl no	**Dye Adsorbed**	**Q_{max} (*Langmuir Model*) mg/g**	**Q_{max} (*Experimental*) mg/g**
1	vBPDP-8(R)@ARS$^-$	400	430.76
2	vBPDP-8(R)@CR^{2-}	510.2	457.76
3	**vBPDP-8(R)@MO$^-$**	**1080**	**1161.78**
4	**vBPDP-8(R)@FL**	**1260**	**1237.41**

Table S4. Natural bonding orbital data of vBPDP and ARS$^-$.

System	**Donor**	**type**	**Acceptor**	**Type**	**$E^{(2)}$ kcal/mol**
vBPDP@ARS$^-$	C 25 - H 70	σ	S 113 - O 114	σ^*	0.05
	C 33 - C 34	π	C 106 - S 113	σ^*	0.10
	O 114	LP (1)	C 25 - H 70	σ^*	1.71
	O 114	LP (2)	C 25 - H 70	σ^*	3.69
	O 114	LP (2)	C 33 - C 34	π^*	3.06
	O 114	LP (3)	C 25 - H 70	σ^*	3.62

	O 116	LP (3)	C 33 - C 34	π*	3.09

Table S5. Natural bonding orbital data of vBPDP and FL.

System	Donor	Type	Acceptor	type	$E^{(2)}$ Kcal/mol
vBPDP@FL	C 28 - H 73	σ	C 95 - O 110	Π*	0.08
	N 53 - H 93	σ	C 107 - O 111	σ*	0.42
	C 54 - H 90	σ	C 108 - H 128	σ*	0.08
	N 53	LP (1)	C 107 - O 111	σ*	0.10
	C 95 - O 110	Π	C 28 - H 73	σ*	1.05
	C 107 - O 111	σ	N 53 - H 93	σ*	0.62
	O 110	LP (1)	C 28 - H 73	σ*	1.82
	O 111	LP (2)	N 53 - H 93	σ*	1.13
	O 111	LP (1)	N 53 - H 93	σ*	0.88

Table S6. Natural bonding orbital data of vMEL and ARS^-.

System	Donor	type	Acceptor	Type	$E^{(2)}$ kcal/mol
vMEL@ARS^-	O 90	LP (1)	C 22 - O 90	σ*	0.55
	O 90	LP (2)	C 20 - C 21	π*	0.91
	O 90	LP (2)	C 21 - C 22	σ*	2.06
	O 90	LP (2)	C 22 - C 23	σ*	0.09
	O 90	LP (2)	C 27 - C 38	σ*	1.81
	O 90	LP (2)	C 27 - C 42	σ*	0.12

Table S7. Natural bonding orbital data of vMEL and ARS^-.

System	Donor	Type	Acceptor	type	E$^{(2)}$ Kcal/mol
Vmel with Fl	C 70 - O 85	σ	C 13 - H 65	σ^*	0.05
	C 70 - O 85	σ	C 37 - H 67	σ^*	0.06
	C 70 - O 85	Π	C 13 - H 65	σ^*	0.69
	C 82 - O 86	Π	C 28 - H 47	σ^*	0.10
	C 82 - O 86	Π	C 29 - N 30	σ^*	0.22
	C 82 - O 86	Π	C 29 - H 46	σ^*	0.63
	O 85	LP (1)	C 13 - H 65	σ^*	2.88
	O 85	LP (1)	C 37 - H 67	σ^*	1.30
	O 85	LP (2)	C 13 - H 65	σ^*	2.52
	O 86	LP (1)	C 29 - H 46	σ^*	2.28

Table S8. Bond critical points of vCOFs and dyes molecules interaction, calculated through the Quantum Theory of Atoms in Molecules (QTAIM) analysis.

System	Interactions	$\rho(r)$	$\nabla^2\rho$	λ_1	λ_2	ε	V(rbcp)	G(rcp)	H(r)
vBPDP and ARS$^-$	O116–H77	0.0030	0.0132	0.0162	-0.0103	0.8943	-0.0014	0.0023	0.0009
	O114–H76	0.0025	0.0130	-0.0003	0.0151	3.8601	-0.0014	0.0023	0.0009
	O114–H140	0.0116	0.0627	0.0936	-0.0153	0.0137	-0.0100	0.0128	0.0028
	Na117–C35	0.0119	0.0945	-0.0059	0.1143	1.3049	-0.0128	0.0182	0.0054
vBPDP and FL	O111–H93	0.04564	0.1365	-0.0713	0.2787	0.0075	-0.0355	0.0348	-0.0007
	O110–H73	0.0166	0.0467	-0.0183	0.0822	0.0700	-0.0117	0.0117	0.0000

vMEL and ARS^{-}	O85–H66	0.0051	0.0189	-0.0046	-0.0041	0.1260	-0.0032	0.0040	0.0008
	O85–H64	0.0048	0.0182	0.0257	-0.0040	0.1441	-0.0030	0.0037	0.0007
	S88–H57	0.0047	0.0123	0.0175	-0.0028	0.2470	-0.0018	0.0024	0.0006
vMEL and FL	O85–H67	0.0180	0.0605	-0.0183	0.0985	0.0769	-0.0133	0.0142	0.0009
	O85–H65	0.0190	0.0539	0.0956	-0.0204	0.0303	-0.0134	0.0134	0.0000
	O86-H46	0.0173	0.0574	-0.0170	0.09387	0.1354	-0.0128	0.0136	0.0008

Table S9. Comparison of this work with other related investigations of ARS^{-}, CR^{2-}, MO^{-} and FL dye capture by various POPs/ COFs adsorbents.

Sl No.	Name of POPs/ COFs	Organic dye	Organic dyes capture capacity (mg g^{-1})	Equilibrium Times	References
1.	vBPDP-8(R)	Alizarin Red S	430.76	1 min	**This work**
		Methyl Orange	**1161.78**	**40 sec**	
		Congo red	457.76	2 min	
		Fluorescein	**1237.40**	**<10 sec**	
2.	vMEL-7(R)	Alizarin Red S	338.46	2 min	**This work**
		Methyl Orange	989.94	2 min	
		Congo red	417.05	3 min	
		Fluorescein	1161.78	60 sec	
3.	iVOFm	Alizarine Red S	-	5 min	1

		Methyl Orange	-	5 min	
4.	COP_1^{++}	Fluorescein	-	4 min	2
5.	COP_1^{+}	Rhodamine B	-	60 min	
6.	XOF-TIB	Methyl Orange	55.71	-	3
		Congo red	3912.69	-	
7.	3D-ionic-COF-1	Methyl Orange	-	30 min	4
8.	PA-COF	Methyl Orange	978.3	-	5
9.	CX4-BD-1 COF	Methyl Orange	-	120	6
	CX4-BD-2 COF	Methyl Orange	-	120	
10.	COP_1^{++}	Congo Red	928	15 min	7
11.	C-$NSA_{Naph}HCP$@Br	Methyl Orange	1010	60 min	8
12.	QUST-iPOP-1	Congo Red	1074.9	90 min	9
		Methyl Orange	300	90 min	
13.	V-CDP	Congo red	323	425 min	10
		Methyl Orange	370	425 min	
14.	CalP	Congo red	348.00	-	11
Dye captured by MOFs adsorbent					
SI No.	**Name of MOFs**	**Organic dye**	**Organic dyes capture capacity (mg g^{-1})**	**Equilibrium Times**	**References**

1.	SCNU-Z1-Cl	Methyl Orange	289.00	26 min	12
		Congo red	632.90	**40 min**	
2.	UiO-66-NH$_2$	Methyl Orange	737.6	4h	13
	CNTs@UiO-66-NH2	Methyl Orange	873.00	4h	
3.	MOF 235	Methyl Orange	477	-	14
4.	triazole-Decorated Silver(I)-based MOF	Methyl Orange	409	40 min	15
		Congo red	254	40 min	
5.	Fe-loaded MOF545(Fe)	Methyl Orange	804	-	16
6.	Ce(Ⅲ)-doped UiO-67	Methyl Orange	401	-	17
7.	Cd-ZIF-8	Methyl Orange	93.24	-	18
8.	ZIF-8	Methyl Orange	45.82	-	18

Table S10. Comparison of this work with other related investigations of ARS$^-$, CR^{2-}, MO$^-$ and FL dye capture by various adsorbents.

Sl No.	**Name of POPs/ COFs**	**Organic dye**	**Organic dyes capture capacity (mg g^{-1})**	**References**
1.	vBPDP-8(R)	Alizarin Red S	**430.76**	**This work**
		Methyl Orange	**1161.78**	
		Congo red	**457.76**	
		Fluorescein	**1237.40**	
2.	CANEX sorbents	Methyl orange	-	19
3.	Activated Carbon	Methyl orange	294.1	20
4.	Zeolite	Congo red	80	21
		Methyl orange	50	
5.	P5-P polymer	Methyl orange	909.0	22
6.	Fe$_3$O$_4$/NiO nanocomposite	Congo red	210.78	23

7.	A-MnO_2	Methyl orange	1488.7	24
8.	Graphene/PANI/Fe_3O_4	Congo red	248.76	25

SVIII: References:

1. Fajal, S. *et al.* Ordered Macro/Microporous Ionic Organic Framework for Efficient Separation of Toxic Pollutants from Water. *Angew. Chem. Int. Ed.* **62**, e202214095 (2023).
2. Das, G. *et al.* Microwave-assisted synthesis of a viologen-based covalent organic polymer with redox-tunable polarity for dye adsorption. *RSC Adv.* **7**, 3594-3598 (2017).
3. Wang, S. *et al.* Tailoring the adsorption properties of imidazole-based halogen bonded organic frameworks for anionic dye removal. *Mater. Chem. Front.* **8**, 4096-4105 (2024).
4. Li, Z. *et al.* Three-Dimensional Ionic Covalent Organic Frameworks for Rapid, Reversible, and Selective Ion Exchange. *J. Am. Chem. Soc.* **139**, 17771-17774 (2017).
5. Leng, H. *et al.* Novel three-dimensional fibrous covalent organic frameworks constructed via silver amalgam bridging for efficient organic dye adsorption and removal. *Nanoscale* **16**, 16026-16034 (2024).
6. Garai, B. *et al.* Taming the Topology of Calix[4]arene-Based 2D-Covalent Organic Frameworks: Interpenetrated vs Noninterpenetrated Frameworks and Their Selective Removal of Cationic Dyes. *J. Am. Chem. Soc.* **143**, 3407-3415 (2021).
7. Skorjanc, T. *et al.* Redox-Responsive Covalent Organic Nanosheets from Viologens and Calix[4]arene for Iodine and Toxic Dye Capture. *Chem. Eur. J.* **24**, 8648-8655 (2018).
8. Shen, X. *et al.* Cationic porous organic polymers as an excellent platform for highly efficient removal of pollutants from water. *J. Mater. Chem. A* **6**, 20653-20658 (2018).
9. Jiao, S. *et al.* Evaluation of an Ionic Porous Organic Polymer for Water Remediation. *ACS Appl. Mater. Interfaces* **13**, 39404-39413 (2021).
10. Skorjanc, T., Shetty, D. & Trabolsi, A. Pollutant removal with organic macrocycle-based covalent organic polymers and frameworks. *Chem* **7**, 882-918 (2021).
11. Shetty, D. *et al.* An ultra-absorbent alkyne-rich porous covalent polycalix[4]arene for water purification. *J. Mater. Chem. A* **5**, 62-66 (2017).
12. Deng, S.-Q. *et al.* Hydrolytically Stable Nanotubular Cationic Metal–Organic Framework for Rapid and Efficient Removal of Toxic Oxo-Anions and Dyes from Water. *Inorg. Chem.* **58**, 2899-2909 (2019).
13. Sang, X. *et al.* Interfacial growth of metal–organic framework on carboxyl-functionalized carbon nanotubes for efficient dye adsorption and separation. *Anal. Methods* **12**, 4534-4540 (2020).
14. Haque, E., Jun, J. W. & Jhung, S. H. Adsorptive removal of methyl orange and methylene blue from aqueous solution with a metal-organic framework material, iron terephthalate (MOF-235). *J. Hazard. Mater.* **185**, 507-511 (2011).
15. Kumar, S. *et al.* Fluorine-Containing Triazole-Decorated Silver(I)-Based Cationic Metal–Organic Framework for Separating Organic Dyes and Removing Oxoanions from Water. *Inorg. Chem.* **60**, 7070-7081 (2021).
16. Zhang, C., Li, H., Li, C. & Li, Z. Fe-Loaded MOF-545(Fe): Peroxidase-Like Activity for Dye Degradation Dyes and High Adsorption for the Removal of Dyes from Wastewater. *Molecules* **25**, 168 (2020).
17. Yang, J.-M. *et al.* Rapid adsorptive removal of cationic and anionic dyes from aqueous solution by a Ce(III)-doped Zr-based metal–organic framework. *Micropor. Mesopor. Mat.* **292**, 109764 (2020).

18. Ba Mohammed, B. *et al.* Insights into methyl orange adsorption behavior on a cadmium zeolitic-imidazolate framework Cd-ZIF-8: A joint experimental and theoretical study. *Arab. J. Chem.* **14**, 102897 (2021).
19. Karan, C. K. & Bhattacharjee, M. Self-Healing and Moldable Metallogels as the Recyclable Materials for Selective Dye Adsorption and Separation. *ACS Appl. Mater. Interfaces* **8**, 5526-5535 (2016).
20. Mohammadi, N., Khani, H., Gupta, V. K., Amereh, E. & Agarwal, S. Adsorption process of methyl orange dye onto mesoporous carbon material–kinetic and thermodynamic studies. *J. Colloid Interface Sci.* **362**, 457-462 (2011).
21. Hamd, A. *et al.* Comprehensive evaluation of zeolite/marine alga nanocomposite in the removal of waste dye from industrial wastewater. *Sci. Rep.* **13**, 8082 (2023).
22. Shi, B. *et al.* A pillar[5]arene-based 3D network polymer for rapid removal of organic micropollutants from water. *J. Mater. Chem. A* **5**, 24217-24222 (2017).
23. Koohi, P., Rahbar-kelishami, A. & Shayesteh, H. Efficient removal of congo red dye using Fe3O4/NiO nanocomposite: Synthesis and characterization. *Environ. Technol. Innov.* **23**, 101559 (2021).
24. Liu, Y., Wei, J., Tian, Y. & Yan, S. The structure–property relationship of manganese oxides: highly efficient removal of methyl orange from aqueous solution. *J. Mater. Chem. A* **3**, 19000-19010 (2015).
25. Genc, R. *et al.* High-Capacitance Hybrid Supercapacitor Based on Multi-Colored Fluorescent Carbon-Dots. *Sci. Rep.* **7**, 11222 (2017).